# LOW-BACKGROUND SCIENCE WITH THE NEXT GENERATION SUPERCDMS HVEV DARK MATTER DETECTOR

By

COREY BATHURST

A DISSERTATION PRESENTED TO THE GRADUATE SCHOOL
OF THE UNIVERSITY OF FLORIDA IN PARTIAL FULFILLMENT
OF THE REQUIREMENTS FOR THE DEGREE OF
DOCTOR OF PHILOSOPHY

UNIVERSITY OF FLORIDA

2023

Dedicated to all my friends and family.

ACKNOWLEDGEMENTS

This thesis owes thanks to all the members of SuperCDMS that have helped me or worked with me through the years. As well as all my friends and colleagues I've made or kept through this period of my life. It was honestly the most difficult time of my life mentally and physically and I would not have made it through without all of you.

TABLE OF CONTENTS

LIST OF FIGURES

Abstract of Dissertation Presented to the Graduate School
of the University of Florida in Partial Fulfillment of the
Requirements for the Degree of Doctor of Philosophy

LOW-BACKGROUND SCIENCE WITH THE NEXT GENERATION SUPERCDMS HVEV DARK MATTER DETECTOR

By

Corey Bathurst

August 2023

Chair: Tarek Saab
Major: Physics

The abundant evidence for missing non-luminous mass, or dark matter, has made it difficult to refute its existence. Nevertheless, detection experiments have failed to find this missing mass. The Super Cryogenic Dark Matter Search(SuperCDMS) experiment aims to directly detect dark matter interactions with standard model particles by measurements of energy deposited in Si/Ge crystal during a scattering or absorption of dark matter. Historically this search focused on dark matter masses in the GeV scale, but continued lack of discovery has pushed dark matter search efforts to lower masses looking for sub-GeV mass dark matter. With this lighter mass comes new challenges in measuring these interactions as energy depositions are smaller, requiring higher sensitivities, and the many-body effects of dark matter interacting with condensed matter becomes more apparent. This thesis covers efforts made in The Ionization Measurement with Phonons At Cryogenic Temperatures (IMPACT) measurement, which characterized the ionization yield of nuclear recoils with sub-keV energies. The IMPACT measurement was able to extend empirical measurements of the yield in Si down to 100 eV. This thesis also covers the analysis and results of the third dark matter search performed by the SuperCDMS collaboration that focused on dark matter interactions with electrons in condensed matter systems. This dark matter search found marked improvement upon the previous two searches in background rejection and limiting setting and provided a clear idea of what can be improved for dark matter-electron searches moving forward.

CHAPTER 1
INTRODUCTION

## 1.1 Early Motivation and Evidence for Dark Matter

For centuries humankind has taken the relations derived by Newton as the fundamental laws of motions that govern how matter evolves with time. In particular this includes his universal law of gravitation that extended upon the Kepler's laws of celestial motion relating the the explicit mass of a body to the gravitational pull it generates and evolution of other masses that orbit. Lifetimes later, Einstein discovers a method to describe the fundamentals of Newton's gravitational law as an approximation to the mathematically intense yet conceptionally elegant relation between mass-energy density and the fundamental structure of the space (spacetime) we live in. This concept is described by general relativity. General relativity has led to predictions such as the existence of black holes, or confirmation of the frame dragging of spacetime measured by the precession of Mercury's orbit around the Sun. It shows that the picture of how mass, or matter as we see, is gravitational related in a more complicated manner than the relation generated by Newton. In more recent times looking out to the cosmos has shown evidence of a need for new physics, or physical constituents, in order to reconcile many observations.

The earliest suggestion for significant quantities of non-luminous matter in the Universe comes from looking at the motion of celestial bodies. The first such hint was generated by Fritz Zwicky in his 1933 paper [1] which extended upon measurements of galactic velocities made by Hubble and Humason [2]. Hubble and Humason noted that eight galaxies in the Coma cluster showed very large velocity dispersions on the order of $10^3$ km/s. Zwicky expanded upon this by estimating the mass of the cluster by counting the number of galaxies and adopting an average galactic mass of $10^9$ solar masses. He then estimated the size of the system and used the Virial theorem to predict that the system should exhibit a dispersion on the order of 80 km/s. He then worked out that in order to achieve this dispersion the amount of mass in the cluster would have to be over 400 times greater than that determined by observations of luminous matter. These calculations were deemed intriguing at the time but as they were the first suggestion of the dominance of non-luminous matter they were not taken as concrete. Similar measurements by

Sinclair Smith in the 1930s on the Virgo cluster suggested a mass-to-light ratio on the order of 200 further adding to this discrepancy.

Uncertainty of the validity of these measurements continued without clarification until the 1970s when Vera Rubin and Kent Ford cataloged observations the radial velocity distribution of M31 as a function of distance from their galactic centers. The importance of this measurement can be seen when again considering the Virial theorem but this time applied to individual galaxies. Generically the Virial theorem can be given for potentials that scale as $V(r) \propto r^n$ as

$$2\langle KE\rangle = -n\langle V\rangle. \tag{1-1}$$

Where $\langle KE\rangle$ is the time averaged kinetic energy and $\langle V\rangle$ is the time averaged potential energy. For a gravitational potential we have $n = 1$. As for the time averaged potential and kinetic energies we have

$$\langle V\rangle = -\alpha\frac{GMm_*}{R} \tag{1-2}$$

and

$$\langle KE\rangle = \frac{1}{2}m_*v_*^2 \tag{1-3}$$

Where $M$ is the mass inside the radius of orbit, $R$, $m_*$ and $v_*$ are the mass and velocity of the orbiting star and $\alpha \leq 1$ is a parameter depending on the mass distribution of the mass inside the radius. This leads us to the proportionality

$$v \propto R^{1/2} \tag{1-4}$$

or that the radial velocity of stars orbiting should steadily fall off with distance. This is in contrast to Rubin and Ford's measurement [3] which showed that at large radii the velocities measured instead remained relatively constant. This effect is shown in Fig. 1-1 in a later paper measuring this same effect with greater precision using a composition of CO, optical, and HI measurements of nearby spiral galaxies with better spatial and velocity resolution. These measurements seem to suggest the requirement for an unseen distribution of mass that follows $M(R) \propto R$ and extends to regions beyond the visible disk of luminous matter. This measurement and a number of others related to the measurable dynamics of individual galaxies [4, 5, 6], marked a major turning point in the history of dark matter as it began to solidify that the astronomical community has a missing point of knowledge and/or that a significant portion of the universe remains unseen.

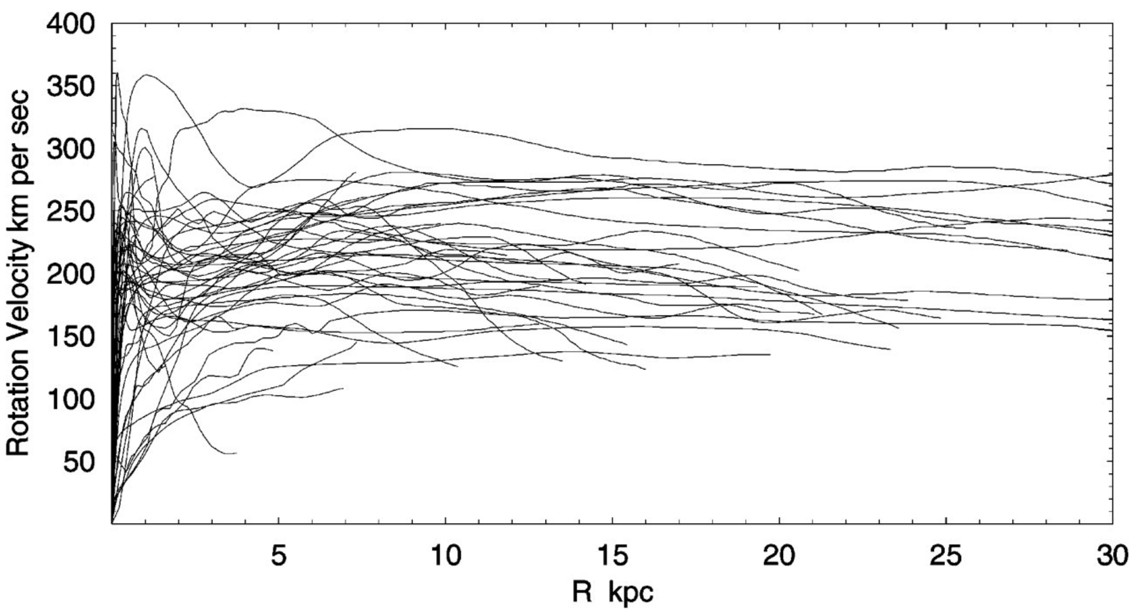


Figure 1-1. Composition of galactic rotation curves for a number of spiral galaxies from Sofie and Rubin as a follow up to the 1970's measurements. The radial velocities flatten instead of falling off with distance as predicted by the Virial theorem. Figure taken from [7].

A potential alternative to non-luminous matter is that our knowledge of laws governing the universe are instead lacking. In particular that our understanding of gravity is incomplete. This is explored in the ideas of modified gravity first put forth by Mordehai Milgrom in 1983 [8] with his postulated MOdified Newtonian Dynamics (MOND) which was effectively a thought experiment towards solving the galactic rotation curve discrepancy by modifying Newton's second law. Milgrom postulated that Newton's second law could be recast as

$$F = m\mu\left(\frac{a}{a_0}\right)a \tag{1-5}$$

Where the modification comes in the form of the function $\mu$ and suggests that Newton's second law deviates from its accepted form in the limit of small accelerations. This function would have a limiting behavior of $\mu \to 1$ as $a/a_0 \ll 1$ and $\mu \to a/a_0$ as $a/a_0 \gg 1$ with this reference acceleration on the order of $a_0 \sim 10^{-10}\mathrm{m/s}^2$. This modification would then be thought to be the limiting case of a more complete theory.

MOND presented a reasonable phenomenological solution to the observed galactic dynamics but had several shortcomings. As this was presented as more of a thought experiment, instead of a rigorous theory, it lacked fundamentals such as following physical conservation laws. This was overcome in a later paper present by Bekenstein and Milgrom [9] in which a more complete version of this modification was produced from a Lagrangian formulation of Newtonian Mechanics to ensure both conservation of energy and momentum for some spherical symmetries in limiting cases. Another glaring issue is that this form had no extension to relativity. The modern form of MOND is presented as Tensor-Vector-Scalar gravity (TeVeS) [10] works an extension to general relativity through the addition of several free parameters. This theory allows for the explanation of more complicated scenarios as compared to its non-relativistic counterpart but fails to accurately model several key modern observations discussed in the following.

A so-called smoking gun for the existence of non-luminous matter in the universe is seen through observations of the Bullet cluster [11]. The Bullet cluster is made of a recent collision of two galaxies in which the major luminous component of plasma is heated through the collision and becomes visible in the X-ray regime. These heated components would then become spatially separated from the non-luminous components not slowed by this collision. The hypothesis is then if this luminous plasma dominates the gravitational mass of the cluster, the observed gravitational potential of the cluster would follow the plasma distribution. This is contrary to what was seen when comparing X-ray observations of the cluster's plasma, and the measured gravitational potential inferred by weak gravitational lensing effects produced by the cluster as seen in Fig. 1-2. In this we see that the major gravitational component of the cluster, largely unaffected by the drag of the collision, is spatially separated from the observed luminous mass.

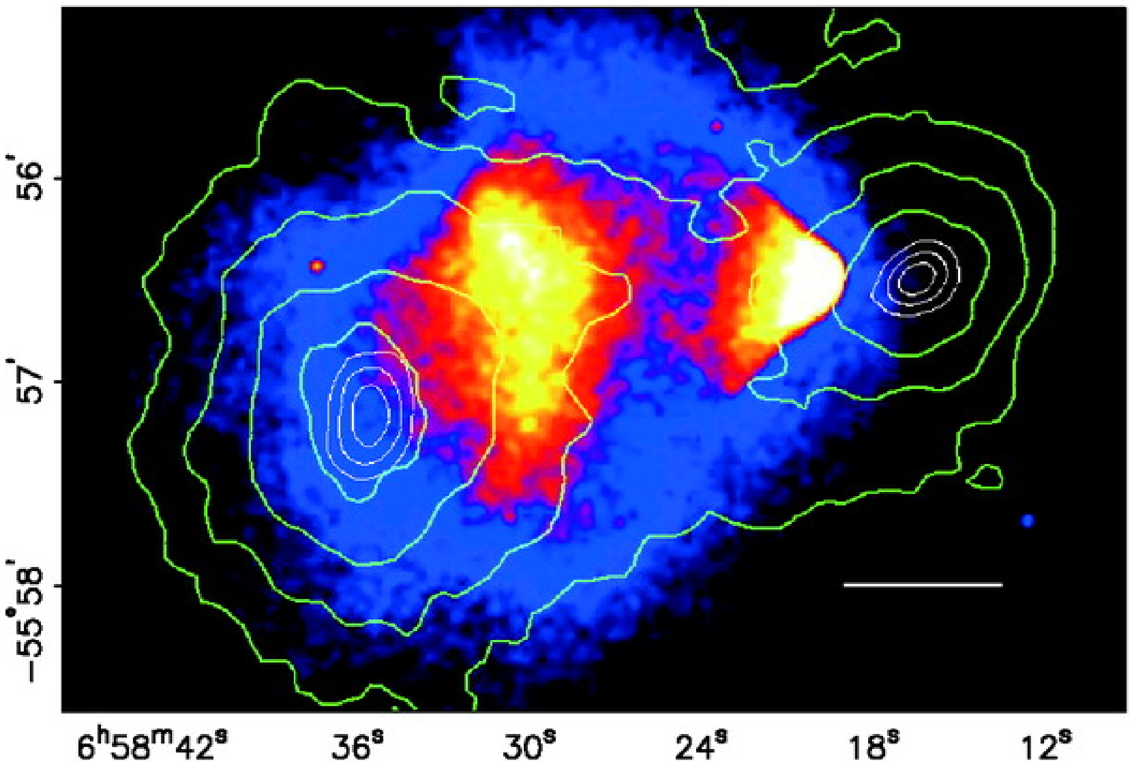


Figure 1-2. An overlay of X-ray measurements taken by Chandra (Heat map) and the inferred mass distribution taken from weak gravitational lensing measurements (green contours) produced by Magellan of the Bullet cluster. This overlay shows a clear spatial separation between the major luminous component and the inferred gravitational mass of the cluster. The white bar indicates 200 kpc. Figure taken from [11].

The final consideration of evidence for missing matter in the universe comes from observations of the Cosmic Microwave Background (CMB) and its incredible match to the standard model of cosmology, the Lambda Cold Dark Matter (ΛCMB) model of cosmology, which takes general relativity as the correct theory of gravity on cosmological scales.

## 1.2 Potential Forms for Dark Matter

Dark matter can exist in the universe as a number of different forms. As elementary particles with fundamental interactions stretching to the early universe, to black holes preventing the electromagnetic interactions of their constituents from escaping their grasp. The fundamental component to dark matter remaining dark is the lack of an electromagnetic component generating standard model photons observable by us. This section discusses some of the theorized forms of dark matter as well as their means of creation.

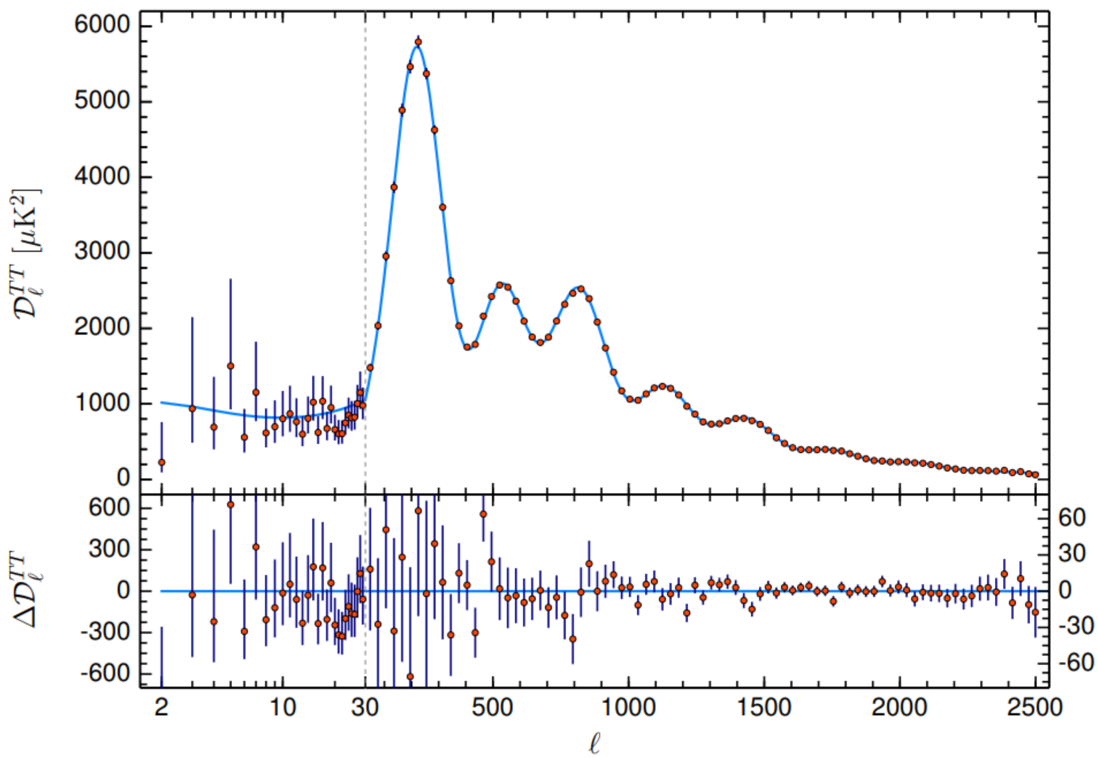


Figure 1-3. (Top) The cosmic microwave background anisotropy as measured by the Planck experiment (red) and the fit to the ΛCMB model (blue) determining relative fractions of dark matter and baryons in the early universe. Explicitly this is the Fourier transform of power spectrum variations at a function of real space. (Bottom) Absolute difference between the measurement and fit. Figure taken from [12].

### 1.2.1 Particle Dark Matter

The most prevalent considered form of dark matter in modern times is that it is its own particle, or class of particles, that has yet to be directly detected. It is thought that the dark matter measured gravitationally in the universe was formed in the early universe and in modern times this production has shut off on a cosmologically significant scale. The mass of some of these particles can be as light as $10^{-22}$ eV and as heavy as $10^{12}$ eV depending on the potential model considered[13, 14, 15, 16].

#### 1.2.1.1 Generation of Dark Matter: Freeze-out

Theories of particle dark matter start with theories of how their measured abundances, known as relic dark matter density, first came to form in the early universe. The first model for

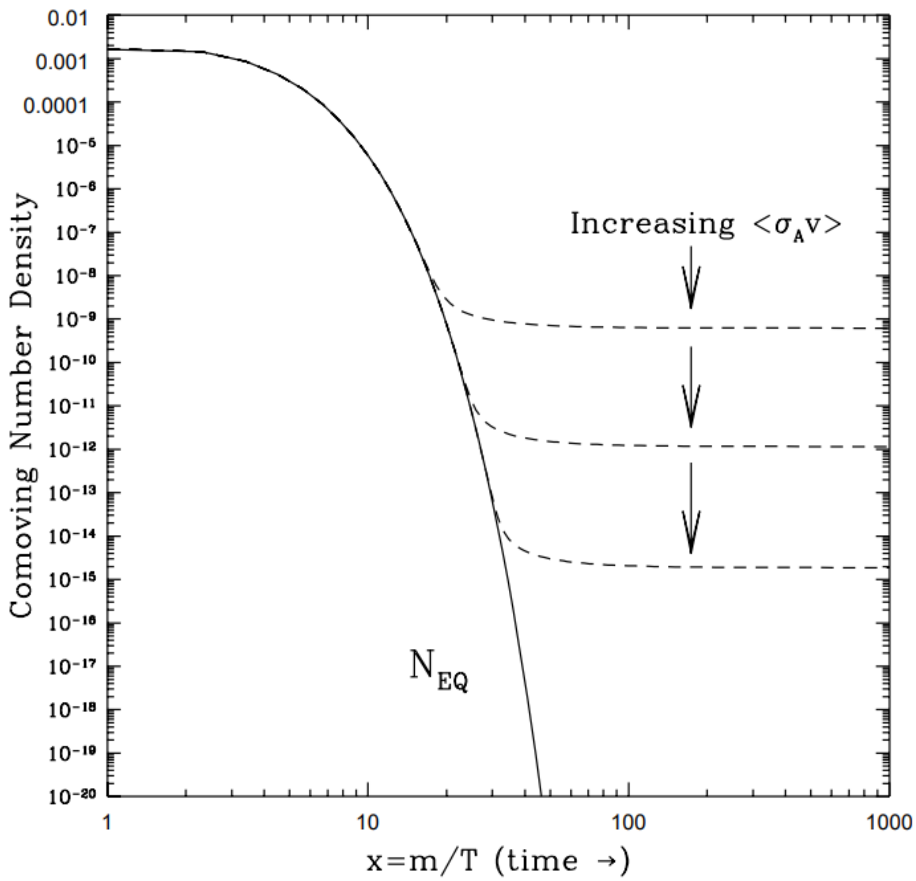


Figure 1-4. The evolution of dark matter number density as a function of time (dark matter mass / temperature of universe). The solid line shows the equilibrium number density denoting creation rates of dark matter and how the number density would tend to zero due to Boltzmann suppression of creation rates as the Universe cools. The dotted lines show how expansion rates surpassing annihilation rates leads to a steady state to the number density. This also shows that with increasing annihilation cross-section comes lower relic density.

dark matter creation assumes that dark matter was in thermal equilibrium with standard model particles in the early universe [17]. During this period annihilation ($\chi\bar{\chi} \rightarrow l\bar{l}$) and production ($l\bar{l} \rightarrow \chi\bar{\chi}$) processes of dark matter occur at equal rates creating and annihilating both dark matter ($\chi$) and standard model (l) particles.

This occurs during the period that the temperature of the universe is greater than the mass of dark matter but as the universe cools the annihilation process begins to shut off. The number density of dark matter ($n_{\chi}$) particles is governed the Boltzmann equation

$$\frac{dn_\chi}{dt} + 3Hn_\chi = -\langle\sigma_A v\rangle[(n_\chi)^2 - (n_\chi^{eq})^2] \tag{1-6}$$

where $H$ is the Hubble parameter, $\langle\sigma_A v\rangle$ is the velocity averaged annihilation cross-section and $n_\chi^{eq}$ is the number density of the particles in thermal equilibrium. This gives in limits of high and low temperature relative to dark matter mass:

$$n_\chi \propto T^3; m_\chi \ll T, \tag{1-7}$$

$$n_\chi \propto T^{3/2}\exp\left(\frac{-m_\chi}{T}\right); m_\chi \gg T. \tag{1-8}$$

This could lead one to assume that as the universe cooled eventually all the relic density would be annihilated away. However, as the universe expanded the expansion rate began to exceed the annihilation rate annihilation instead shuts off and leaves a remaining relic density. This period of time when annihilation stops and the density becomes largely constant is the idea of the 'Freeze-out'. The evolution of dark matter density in this model is show in Fig. 1-4.

When the freeze-out criteria is met, the Boltzmann equation reduces to

$$Hn_\chi = \langle\sigma_A v\rangle(n_\chi)^2. \tag{1-9}$$

Using this in combination with the conserved quantity $n_\chi/s$, where $s$ is the entropy density, and the freeze-out temperature of $T_f \approx m_\chi/20$, the present day mass density can be written as

$$\Omega_\chi h^2 \approx \left(\frac{3\times10^{-27}\mathrm{cm}^3\mathrm{s}^{-1}}{\langle\sigma_A v\rangle}\right). \tag{1-10}$$

This implies with a DM density of $\Omega_\chi h^2 \sim 0.1$, that velocity averaged annihilation cross-section should be on the order of $10^{-28}\mathrm{cm}^2\mathrm{s}^{-1}$.

#### 1.2.1.2 WIMPs

The long standing well motivated particle candidate for DM are the Weakly Interacting Massive Particles (WIMPs). These particles arise in supersymmetric theory [15], and particularly interesting when considering the annihilation cross-section predicted by the freeze-out model. WIMPs are expected to interact on the weak scale where $\langle \sigma_A v \rangle \sim 10^{-25} \mathrm{cm}^2 \mathrm{s}^{-1}$. This is particularly close to the estimate of the DM cross-section and therefore place WIMPs as a reasonable DM candidate.

WIMPs are predicted to have masses on the order of GeV to TeV, which is convenient as this gives individual DM particles enough energy and momentum to be able to cause measurable nuclear recoils when interacting with standard model particles. At this level of interaction, any many body effects are negligible and the interaction can be considered a classical elastic scattering between the DM and a nuclei.

For decades a number of experiments have been performed to try and look for these interactions to no avail. While this has not completely ruled out WIMPs as a DM candidate, it has motivated the scientific community to broaden the DM search. In particular, this means looking to lighter DM candidate particles with masses less than a GeV.

#### 1.2.1.3 Sub-GeV Dark Matter

Though much focus has been on WIMPs throughout last few decades, theory has presented a multitude of possibilities for the form of a particle DM candidate. A summary of all these possibilities and their potential masses is shown in Figure 1-5. Many experiments, including SuperCDMS, have begun to look to lighter candidate particles, which is referred to in this evolving field very broadly as 'Sub-GeV DM.' A large focus in this class of candidates is Hidden Sector DM (also sometimes called Dark Sector DM).

This type of DM assumes that DM interacts with SM particles through a new force mediator. This is because all SM forces are ruled out for DM masses at this scale; electromagnetic/strong interactions would of course produce light, and the weak mediated interaction cross-section no longer matches for DM masses in this scale. This form of DM can

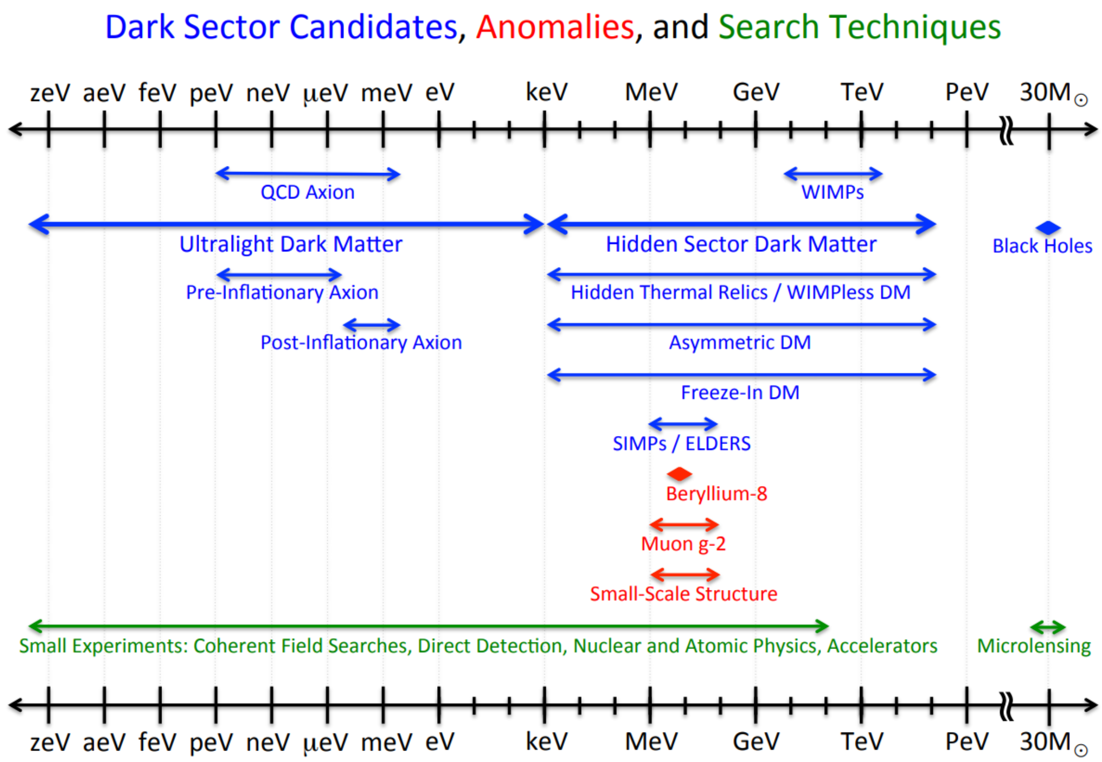


Figure 1-5. An overview of the majority of all non-baryonic dark matter candidates ever considered (blue), the scale some anomalies occur at (red) and give some credence to some of these models, and finally the energy scales at which different experiments could operate to search for some of these candidates (green).

also be comprised of a number of different particles [18, 19, 20] thus the namesake of 'sector.' A benchmark model in this class is the 'dark photon' model. In this model the hidden sector is minimally made up of a massive dark matter particle, and the dark photon which mediates the dark matter interaction with the standard model. The dark photon can be massive unlike the electromagnetic case.

Looking to even lighter masses, bosonic DM candidates can have masses in the sub-keV regime. These types of DM are referred to as 'ultralight' DM. This includes the so call 'Axion-Like Particle' (ALP) which follow the model of the Quantum Chromodynamics (QCD) axion. The QCD axion was introduced there to solve the strong CP problem [21, 22, 23]. These can exist in the mass range of roughly $10^{-12}$ eV to $10^{-2}$ eV, but more broadly ultralight DM can exist all the way down to $10^{-22}$ eV.

### 1.2.2 Other Possibilities

Though most baryonic DM candidates have been ruled out, a few possibilities still remain. To quickly overview these:

1. MAssive Compact Halo Objects (MACHOs): This considers the possibility of DM being made up compact objects having small luminosities such as planets, brown dwarfs, neutron stars, or black holes. The MACHO collaboration search looked for signatures of these objects in the Milky Way and found an upper limit on the DM fraction these could constitute as 8%. This is likely an overestimate still as given by the CMB measurement of Baryon fraction [24].

2. Primordial Black Holes: These are black holes created in modified inflation scenarios. Much of the possible mass ranges in for this have been ruled out [25]. This form of DM require significant modifications to the standard model of early universe cosmology, but this possibility cannot be fully ruled out with current constraints on inflation[24].

The brevity of this list shows the amount of effort that has been put forth in shortening the possible sources of baryonic DM. Though still plausible, the lack of evidence for baryonic DM points to the need for new physics beyond the standard model.

## 1.3 Methods of Dark Matter Detection

Now that I've established some of the potential forms of DM, I'll overview the methods of detection for these. This can be broken into three classes: production of DM, indirect detection of DM, and direct detection of DM.

### 1.3.1 Production

Attempts at detection of production of DM occur at high-energy colliders. The weakness of interaction DM has makes it so that any DM produced in a collider would not be measurable, and DM produced would simply pass through the collider. Therefore instead of directly looking for DM, production experiments look for missing energy and momentum in collision events, marking the production of an undetectable particle. These types of experiments are referred to as mono-X experiments, where X stands for a standard model particle [26]. So far these types of experiments have only returned results consistent with standard model physics, in other words have not found any signature of DM particles[27, 28].

A second method used at colliders are beam dump experiments. In these experiments proton beams are fired at a dense target material and have a chance to produce DM particles. These DM particles then have a chance to be detected at a secondary detector downstream from the production point. These experiments have been used to set limits on DM interaction parameters [29]. This means of DM detection is a mixture of production and direct detection.

### 1.3.2 Indirect

Methods of indirect detection focus on looking for products of DM interactions. By looking at places of high DM density, such as the galactic center, comparisons of the amount of measured flux of different particles to the expected amount can look for discrepancies that might point to DM. Searches of this manner typically look for high energy photons [30, 31], cosmic rays [32, 33], or neutrinos [34].

Additional methods of indirect detection look for effects of DM at the cosmological scale. Interactions with or decays to standard model particles in the early universe could alter the thermal history of DM in a measurable way. Looking for difference in say the expected spectrum of the CMB is a way of looking for DM signatures.

### 1.3.3 Direct

Direct detection of DM looks for interactions of DM with standard model particles by measurements of energy depositions in the absorption or scattering. As this is centric to the physics discussed in this thesis, I'll describe these interactions in more detail. Historically direct detection experiments have looked for nuclear recoils with atomic, molecular, or condensed matter systems. These interactions have a differential event rate per recoil energy per target exposure is of the form [35]

$$\frac{\mathrm{d}R}{\mathrm{d}E_R} = \frac{N m_N}{2\mu_{N\chi}^2 m_\chi} \frac{\mathrm{d}\sigma}{\mathrm{d}E_R} \rho_\chi \int_{v_{\min}}^{v_{\max}} \mathrm{d}^3 v \frac{f(\mathbf{v})}{v}. \tag{1-11}$$

This differential rate depends on the degree DM interacts with the standard model, the physical properties of both pieces in the interaction, and the frequency with which DM has an opportunity to interact with the target. Specifically this is the mass of both the target nuclei ($m_N$) and DM ($m_\chi$), the number of target nuclei ($N$), the reduced mass of the system ($\mu_{N\chi}$), the cross-section of interaction ($\sigma$), the local DM density ($\rho_\chi$), and the velocity distribution ($f(\mathbf{v})$) DM follows.

The local density and dynamics of DM come from astrophysical observations and simulations [36, 37]. These assume that DM is distributed surround the galaxy isotropically and isothermally following the Standard Halo Model (SHM), and the velocities follow a Maxwell-Boltzmann distribution. The boundaries of this distribution are truncated at the minimum velocity a given DM mass must have to impart the given recoil energy and the maximum is set by the galactic escape velocity.

The interaction cross-section as a function of DM mass defines the parameter space where direct detection experiments first look to exclude parts of this space, narrowing down the potential forms of DM. The differential form of the cross-section is [15]

$$\frac{\mathrm{d}\sigma}{\mathrm{d}E_R} = \frac{m_N \sigma_0}{4\mu_{N\chi}^2 v^2} F^2(q), \tag{1-12}$$

where $F(q)$ is a momentum transfer dependent nuclear form factor and $\sigma_0$ is a zero-momentum transfer scattering cross-section which in the spin-independent case (which most experiments focus on) takes the form

$$\sigma_0^{(\mathrm{SI})} = \frac{4\mu_{N\chi}^2}{\pi}(Zf_p + (A-Z)f_n)^2. \tag{1-13}$$

$Z$ and $A$ are the atomic number and atomic mass of the interacting nuclei and $f_{p,n}$ are coupling constants between DM and protons and neutrons. These couplings are assumed to be the same by most, leaving an $A^2$ scaling of $\sigma_0$. This is the basis of many experiments favoring using heavier nuclei such as xenon.

In searches for sub-GeV DM, the interaction energies are much smaller and nuclear recoil experiments become insensitive to these. In this case, DM search experiments instead look for interactions with electrons in condensed matter systems. The differential rate for electronic recoils is notably more complex than for nuclei recoils [38, 39**?** , 40],

$$\frac{\mathrm{d}R}{\mathrm{d}\ln E_R} = \frac{N_T \alpha m_e^2}{2\mu_{\chi e}^2} \bar{\sigma}_e \frac{\rho_\chi}{m_\chi} \int_{v_{\min}}^{v_{\max}} \mathrm{d}^3 v \mathrm{d}\ln q \frac{E_R}{q} F_{DM}^2(q) f_{\mathrm{crystal}}^2(q, E_R) \frac{f(\mathbf{v})}{v}. \tag{1-14}$$

Here the subscript $e$ refers to electrons and the extra term in the integral $f_{\mathrm{crystal}}$ is a target dependent crystal form factor that takes into account the band structure of electron states. The momentum dependent form factor $F_{DM}$ in this case is 1 for heavy dark matter mediators and is proportional to $q^{-2}$ for light mediators.

Finally the last form of DM interaction with a condensed matter system I consider is absorption of DM. This occurs in a similar manner to the photoelectric effect, where in this case a DM particle is absorbed and causes ionization. The cases I consider here are the dark photon ($A'$) and ALPs ($a$) discussed in Section 1.2.1.3. The former case kinetically mixes with standard model photons and assumes that standard model particles have a form of dark charge that is the response to this field which is parameterized by a mixing parameter $\varepsilon$ and standard model particles having an electromagnetic charge of $Qe$ to also have a dark charge of $\varepsilon Qe$. This case leads to an interaction rate per target exposure of the form [41]

$$R = \frac{1}{\rho_T} \frac{\rho_\chi}{m_{A'}} \varepsilon_{\mathrm{eff}}^2 \sigma_1(m_{A'}) \tag{1-15}$$

where $\rho_T$ denotes the density of the target, $\sigma_1$ is the real part of the target material's complex conductivity and $\varepsilon_{\mathrm{eff}}$ is the effective mixing parameter modulated from the free space mixing parameter by in-target material space effects to have the form [42, 23]

$$\varepsilon_{\mathrm{eff}}^2 = \frac{\varepsilon^2 m_\chi^2}{(m_\chi^2 - 2m_\chi \sigma_2 + \sigma_2^2 + \sigma_1^2)}, \tag{1-16}$$

where $\sigma_2$ is the imaginary part of the target material's complex conductivity.

In a similar manner the rate of interaction for ALPs with a condensed matter target can be given by [21, 22]

$$R = \rho_\chi \frac{3g_{\chi e}^2 m_\chi}{16\pi\alpha m_e^2}\sigma_{\rm pe}(m_\chi) \tag{1-17}$$

where in a similar manner to the dark photon mixing parameter, $g_{\chi e}$ is the interaction coupling parameter between an ALP and an electron in the target material and $\sigma_{\rm pe}$ is the photoelectric cross-section for the target material.

## 1.4 The Super Cryogenic Dark Matter Search Experiment

The Super Cryogenic Dark Matter Search (SuperCDMS) experiment is a nuclear recoil dark matter search experiment that searches for energy depositions in Si and Ge crystals held at cryogenic temperatures. The experiment has been through a number of generations, with the previous generation at Soudan producing world leading dark matter nuclear interaction limits at the time [43]. SuperCDMS at Soudan ran the interleaved Z-sensitive Ionization and Phonon (iZIP) detectors which utilize both phonon and ionization signals of events registered in the detector to be able to reconstruct positional and energy of these. This detector design excels at background rejection which comes largely in the form of electronic interaction by looking at the difference in response between the ionization and phonon channels. This design works well for dark matter masses $\geq$ 10 GeV however begins to lose sensitivity for lower masses as the average imparted energy decreases as discussed in Section 1.3.3. This motivates optimization of the SuperCDMS detector design towards sensitivity of lower energy interactions and is the focus of the upcoming generation, SuperCDMS SNOLAB.

SuperCDMS SNOLAB is currently under development at the SNOLAB facility located approximately 2 km below the surface in a mine at Sudbury, Ontario, Canada [44]. This facility is designed to house an ultraclean experimental environment for experiments that require low background rates from both atmospheric and local environmental sources. The overall facility standard is enhanced further by shielding employed by SuperCDMS as shown in fig. 1-6.

This generation of SuperCDMS takes lessons learned at Soudan and will utilize two detectors types, iZIP and High Voltage (HV). The HV detectors use the same phonon channel design as the iZIP detectors. They however operate at a high voltage ($\sim$100 V) and forsake the

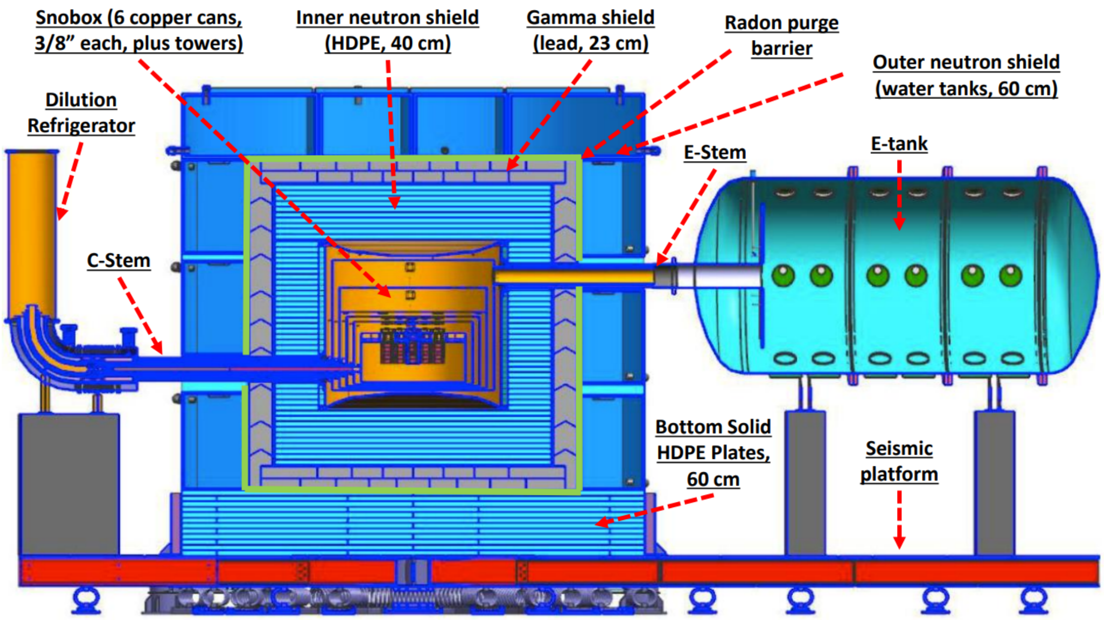


Figure 1-6. The experimental shielding and cryostat layers for SuperCDMS SNOLAB provide protection from local background signals. The entire assembly is placed on top a seismic platform to dampen vibrations from seismic events.

ionization channels completely. The physics of the phonon sensors are described in Chapter 2. The high voltage mode of the phonon channels allows for greater amplification of smaller signals in the detector and therefore improved sensitivity to the lower energy scale expected for lighter dark matter masses [45].

The first phase of SuperCDMS SNOLAB will include 24 detectors separated into 4 towers (stacks). This will include 10(2) iZIP detectors using Ge(Si) crystals and 8(4) HV detectors using Ge(Si) crystals [46]. Each crystal is cylindrical in shape with 100 mm diameter and 33.3 mm thickness. This generation of iZIP detectors have six phonon channels and two ionization channels on each face. They are to be operated with voltage biases of 5-10 V and are designed to be sensitive to DM masses $>$5 GeV. The HV detectors will have six phonon channels on each face as well. They will be operated at $\sim$ 100 V and are designed to have sensitivity to DM masses as low as 300 MeV. The combined operation of both detector types allows SuperCDMS to explore new parameter space and even reach the coherent neutrino scattering floor below 10 GeV [45].

# CHAPTER 2
# DETECTOR PHYSICS

## 2.1 SuperCDMS HV(eV) Detector Overview

The SuperCDMS HV(eV) detectors are essentially phonon calorimeters. The phonon signals generated in the Si / Ge crystals are a combination of so called prompt photons generated from the initial recoil and athermal luke phonons created by electron-hole pair excitations as they drift across the crystal by the large potential difference ($\sim$100 V) held between the top and bottom instrumented faces. This amplification of phonon energy is governed by the Neganov-Trofimov-Luke (NTL) effect and allows for complete conversion of the recoil to the phonon system. This energy is read out by Quasiparticle-trap-assisted Electrothermal feedback Transition edge sensors (QETs). These sensors are made up of three distinct regions:

1. Superconducting aluminum fins that collect the phonon energy from the crystal by breaking of Cooper pairs into quasiparticles.

2. An overlapping region of aluminum and tungsten that trap these quasiparticles and funnel these excitations into the tungsten.

3. Tungsten voltage biased in the middle of its superconducting transition such that the heat transferred from the quasiparticles pushes the element to the normal state resulting in a sharp change in resistance and thereby a measurable change in the bias current. This design is known as a transition edge sensor (TES).

The entire detector is held in a thermal bath much lower than the tungsten superconducting transition allowing for quick recovery back to the mid-transition state. A schematic of this design is shown in Fig. 2-1. This chapter discusses the specifics and elements for optimization of this design and the additional readout that further amplifies and records the TES signal.

## 2.2 Amplification of Recoil Signals

Any interaction in the Si/Ge crystal will create a population of phonons and have the possibility of producing electron-hole pair excitations. The HV(eV) detector design amplifies and

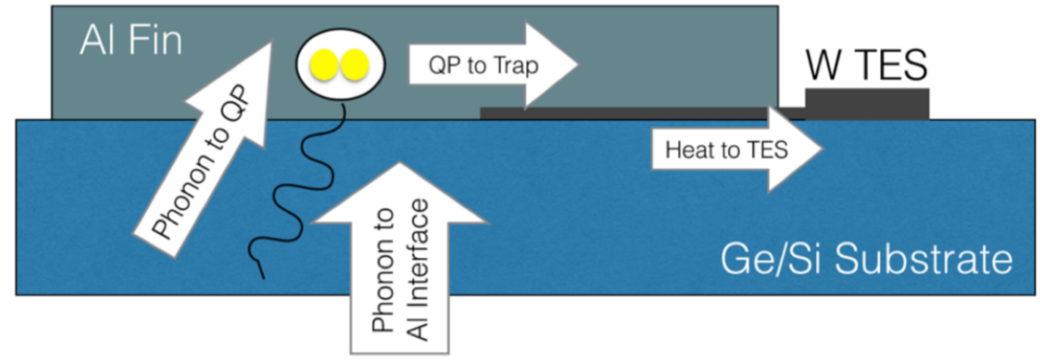


Figure 2-1. A schematic of the HV(eV) detector design. Energy flows from the detector crystal in the form of phonons which break up cooper pairs in the aluminum fins into quasiparticles. These quasiparticles are then caught in the trapping region and funneled into the Transition Edge Sensor (TES). This figure is adapted from [47].

converts this charge excitation to phonon energy by application of a voltage across the crystal which causes the charges to drift towards and away from the QET instrumented faces. The total measured energy signal ($E_{ph}$) as a result of this is given by

$$E_{ph} = E_r + en_{eh}V \tag{2-1}$$

where $E_r$ is the initial recoil energy, $n_{eh}$ is the number of electron-hole pairs generated, and $V$ is the voltage applied across the crystal. The second term, referred to as the NTL gain, is a simple consequence of conversation of energy of the electrons and holes travelling across the entire potential difference. This is shown schematically in Fig. 2-2. The number of electron-hole pairs created on average is a function of the initial recoil energy:

$$n_{eh}(E_r) = y(E_r)\frac{E_r}{\varepsilon_{eh}} \tag{2-2}$$

where $\varepsilon_{eh}$ is the average energy required to create an electron-hole pair in the crystal and $y(E_r)$ is a ionization yield function that takes a value of 1 for electron recoils and a value of 0 to 0.3 for nuclear recoils. The exact form of this yield for nuclear recoils is found from Lindhard

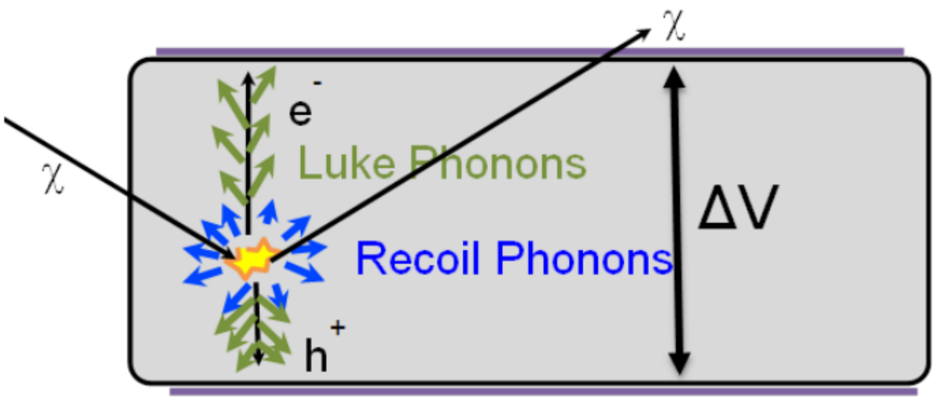


Figure 2-2. A schematic view of the total phonon generation produced in an HV(eV) detector [47]. The total measured energy is a combination of prompt phonons generated from the actual recoil and the luke phonons generated as the charges drift across the crystal.

theory [48] for recoil energies of a few keV and above, but deviates from this for lower energies and is an area of active research. This thesis work contains efforts towards empirically describing this yield down to the 100 eV range through the SuperCDMS IMPACT measurement discussed in Chapter 3. Combining equations (2-1) and (2-2) we have a form for the total phonon energy of

$$E_{ph} = E_r \left(1 + eV\frac{y(E_r)}{\varepsilon_{eh}}\right). \tag{2-3}$$

## 2.3 QETs

The purpose of the QET is to collect as much of the phonon energy created by an interaction as possible while maintaining a precise measure of the energy of an interaction for a wide enough range of interaction energy. Difficulty in achieving this occurs from the energy conversion efficiencies seen at the interfaces between the materials constituting the QET, as well as the decided geometries of the different components. This is additionally complicated by the limits of manufacturing that complicate the reliability of producing an ideal design.

### 2.3.1 Al Fins and Phonon Energy Collection

Phonon readout is mediated by the collection of phonons by the QET's Al fins. These fins collect the phonon energy and as a result break superconducting Cooper pairs into quasiparticle excitations. The most important aspect of these fins is their efficiency in collecting the phonon energy generated in the crystal, giving the most accurate representation of the energy generated by an event as well as that generated by the NTL amplification. One might simply assume that covering the surface of the crystal with as much Al as possible would result in the best phonon collection. In practice this is not true because quasiparticles generated in the Al have a limited diffusion length $l_{\rm diff}$ implying that quasiparticles generated in fins further than a few diffusive lengths are unlikely to make it to the TES overlap region. The diffusion length is given approximately by

$$l_{\rm diff} \sim \sqrt{D\tau_{\rm qp}} \tag{2-4}$$

where $D$ is the quasiparticle diffusivity and $\tau_{\rm qp}$ is the quasiparticle lifetime. Both of these quantities depend on the thickness of the Al fin and this is therefore a major consideration in Al fin design. In addition to concerns of quasiparticles making it to the TES overlap, the overall QET design must also consider the Al lines that bias the TES and are considered 'dead' Al. This requirement intrinsically contributes the divisions of the Al fins depending on the number of TES instrumented on the surface. Finally considerations must also be made in regards to trapped flux vortices in the Al fins. Bulk Al is a type 1 superconductor and typically does not permit bulk magnetic flux lines. Thin film samples of Al however have been shown to support some level of flux vortices. This again implies that considering thicker films may be advantageous. Recent detector designs have also implemented thin slits in the Al fins to reduce the chance of these vortices.

The junction between the Al fin and TES provide an important component of the QET by trapping quasiparticles generated in the Al fins such that it is not energetically favorable for them to travel back into the Al fin region. This is due to proximity effects between the Al and W creating a smaller superconducting band gap than in the Al but also greater than in the W alone. This causes quasiparticles moving into the overlap to shed phonon reducing the energy of those excitations as well as creating other quasiparticles. As such these excitations no longer have the energy on average to move back into the Al region and energy is effectively funneled into the W by the even lower energy of excitations in the W.

To summarize, as energy travels between the different components there are efficiencies in the transfer between the interfaces and as a result an overall energy collection efficiency of the detector . The first is the efficiency of phonon to quasiparticle conversion at the crystal-Al interface. Kaplan downconversion limits this to a maximum of 52%. This collection is further reduced by incomplete Al coverage allowing for energy loss in the crystal or absorption by components other than the active Al. Then is the quasiparticle collection efficiency which depends on the fin aspect ratio, length and thickness. Finally is the efficiency of trapped quasiparticles to the TES. An estimate of this based off iZIP generation 4 detectors finds this to be ∼62% [49]. Overall, in the best case scenario, this gives a maximum collection efficiency of ∼30%.

### 2.3.2 TES

The TES is effectively the calorimeter of the QET that takes advantage of the narrow width (∼0.1 mK) of the superconducting transition of tungsten. At bath temperatures the TES is completely in the superconducting state. The TES is then voltage biased such that it is Joule heated to the middle of its transition between superconducting and normal states. This makes it such that the heat injected by the quasiparticles trapped in the overlap region drive the W normal causing a large change in resistance. This change in resistance causes a drop in bias current through the TES which is then amplified by a Superconducting Quantum Interference Device (SQUID) and readout.

The TES is made up of a thin film (∼2-3 $\mu$m) of W which have crystal phases with superconducting transition temperatures ($T_c$) of 15 mK for the $\alpha$ phase and 1-4 K for the $\beta$ phase. By tuning the mixture of these phases we can mediate $T_c$ to somewhere in-between the two. In practice however the nature of growing thin layers of these phases in production of the TES can alter if a specific phase is maintained as well as introduce proximity effects altering the $T_c$. Actual $T_c$ of SuperCDMS TES have been measured to be more around 50 mK.

The basis of the operation of the TES is on the sharp change in resistance as it moves through its superconducting transition. This is a function of both temperature and current and can be linearized around the transition,

$$R(I,T) \simeq R_0 + \left(\frac{\partial R}{\partial T}\right)_{I_0} \delta T + \left(\frac{\partial R}{\partial I}\right)_{T_0} \delta I. \tag{2-5}$$

The subscript 0 indicates the values of each at the operating point in transition. It is common to rewrite this linearization in terms of two dimensionless parameters [50],

$$\alpha = \frac{T_0}{R_0}\left(\frac{\partial R}{\partial T}\right)_{I_0}, \tag{2-6}$$

$$\beta = \frac{I_0}{R_0}\left(\frac{\partial R}{\partial I}\right)_{T_0}, \tag{2-7}$$

such that

$$R(I,T) \simeq R_0\left(1 + \alpha\frac{\delta T}{T_0} + \beta\frac{\delta I}{I_0}\right) \tag{2-8}$$

As each parameter is essentially the slope of the superconducting transition as a function of each, it is ideal that $\alpha$ is large and $\beta$ tends towards zero so that the response to injected heat is strong but the changing current as resistance changes doesn't add any non-linearity to the thermal response.

After the TES heats up, the system must dissipate this energy so that the TES can return to equilibrium and be functional for further energy depositions. The ability to do this quickly is owed to the reduction in Joule heating as the resistance of the TES increases. The reduction in bias current allows the cooling power of the bath to quickly return the system back to the operational state. Thus the term electrothermal feedback. The differential equation governing the energy flow in the TES requires a balance between the input power of the energy deposition, the Joule heating of the bias current, and the cooling power of the bath. The characteristic time scale of response of the TES and the amplitude change of bias current can result in an oscillatory response in cooling the TES, generating addition noise in the detector [47].

## 2.4 TES Readout

The TES circuit consists of two parallel branches, one including a shunt resistor and the other containing both the TES and the SQUID input coil. The shunt branch is referred to as the

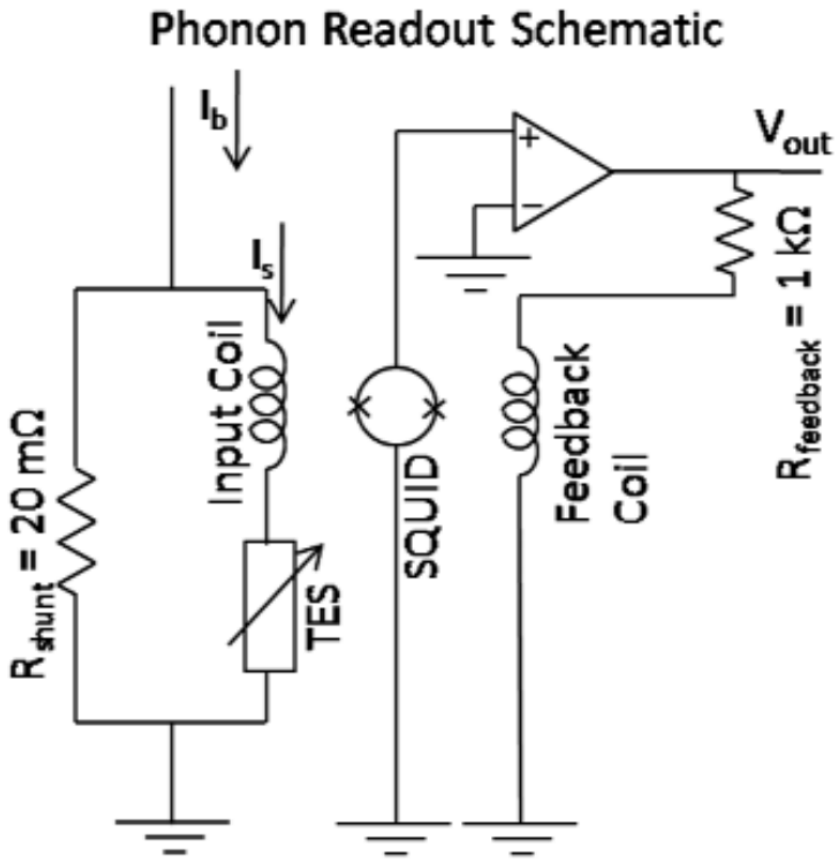


Figure 2-3. The characteristic phonon channel readout circuitry. The two major components are the TES circuit side containing the TES branch and the bias branch controlling the current response to the voltage bias, and the readout circuit which is centered around the SQUID amplification of the TES circuitry by the inductive coupling between the input coil and the SQUID.

bias branch as it controls the bias current resulting from the voltage biasing. The TES branch is referred to as the signal branch. The SQUID input coil is inductively coupled to the readout circuit, comprised of the SQUID, an operational amplifier, and a feedback loop that feeds the input coil response back into the SQUID, maintaining a constant operation point in the SQUID. The circuit diagram of the TES readout is shown in fig. 2-3.

The SQUID is essentially a very sensitive magnetometer that is sensitive to the change in magnetic field through the SQUID loop. The SQUID loop is made up of a loop of superconducting material with a thin film of insulator placed in each branch. The loop tries to maintain the magnetic flux through it due to the Meissner effect. This causes a circulation current in that is measurable as the Josephson current, or voltage, resulting from the tunneling between the two superconducting materials on each of the insulator. This current amplified and readout, as well as fed back into the SQUID itself to regulate the SQUID response in a linear regime.

# CHAPTER 3
# THE IMPACT MEASUREMENT

The ionization yield of the HVeV detector chip material (Si/Ge) is an essential quantity for nuclear recoil dark matter experiments. This can be described theoretically in the keV range by Lindhard theory [48] and measurements agree well in this range (down to 4 keV). In the sub-GeV dark matter mass range, recoil energies reach into the eV scale where yield measurements begin to deviate from Lindhard theory. It therefore becomes important to develop an empirical model for the ionization yield down to these small interaction energies to be able to accurately reconstruct the energies of these interactions. The Ionization Measurement with Phonons At Cryogenic Temperatures (IMPACT) measurement completed at Triangle Universities National Laboratory (TUNL) aimed to determine the ionization yield of Si down to 100 eV, enabling the full reach of expected interactions to be seen in the SuperCDMS at SNOLAB experiment. This chapter describes the IMPACT measurement taken at TUNL, and introduces the general data analysis process of signals measured by HVeV detectors.

## 3.1 The IMPACT Measurement

The IMPACT measurement determines the ionization yield by comparing the phonon energy measured in the HVeV detector to the recoil energy of a known scatterer beamed onto the detector. The expression for the yield in terms of these quantities can be found by rearranging 2-3 to give

$$Y(E_r) = \frac{\varepsilon_{eh}}{eV}\left(\frac{E_{ph}}{E_r} - 1\right). \tag{3-1}$$

IMPACT at TUNL employed a neutron beam of known energy aimed at the HVeV detector to generate recoils between neutrons and Si nuclei. This interaction is classical two-body scattering problem and therefore the recoil energy of the interaction can be measured by determining the scattering angle ($\theta$) of the neutron. The relation between the scattering angle and recoil energy is described by

$$E_r = 2E_n \frac{m_n^2}{(m_n + m_N)^2} \left( \frac{m_N}{m_n} + \sin^2\theta - \cos\theta \sqrt{\left(\frac{m_N}{m_n}\right)^2 - \sin^2\theta} \right) \tag{3-2}$$

where the subscripts n and N refer to the neutron and target nucleus respectively. The IMPACT measurement placed liquid scintillators combined with photomultiplier tubes (PMTs) at specific scattering angles to measure $\theta$. The difficulty then comes in identifying events in both the Si detector and a liquid scintillator through precise timing in both systems to determine coincident events as the same scatterer.

$$\sigma_Y = \frac{\varepsilon_{eh}}{eV} \frac{\sqrt{E_r^2 \sigma_{ph}^2 + E_{ph}^2 \sigma_r^2}}{E_r^2}. \tag{3-3}$$

## 3.2 Experimental Setup

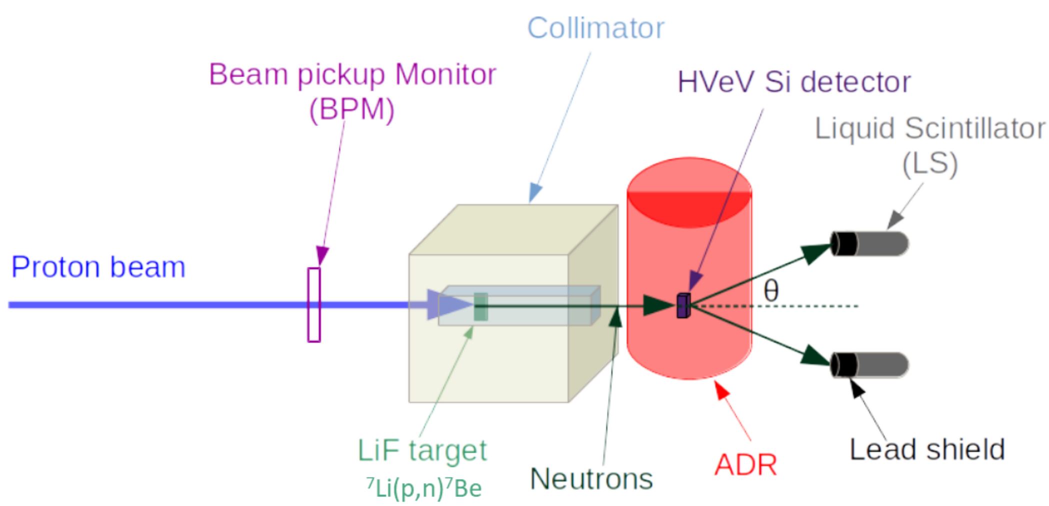


Figure 3-1. A schematic picture of the experimental setup used in IMPACT at TUNL. A missing component in this schematic is the 3 lone wolf PMTs placed directly against the ADR.

The IMPACT experimental setups is shown schematically in Figure 3-1. This measurement system is made up of three major components: the proton beam, the HVeV detector, and the liquid scintillator detector. The proton beam is incident upon a LiF target which in turn produces a neutron beam. This neutron beam is collimated and shines upon the HVeV detector which scatters with nuclei in the detector crystal. In scattering, the neutrons exit the detector at varying angles dependent upon the energy deposited on the crystal. These scattered neutrons are then detected by photomultiplier tubes which are placed in two concentric rings a distance behind the detector, as well three additional tubes placed at varying angles directly against the detector. This section goes into the specifics of each of these major components.

### 3.2.1 Proton Beam

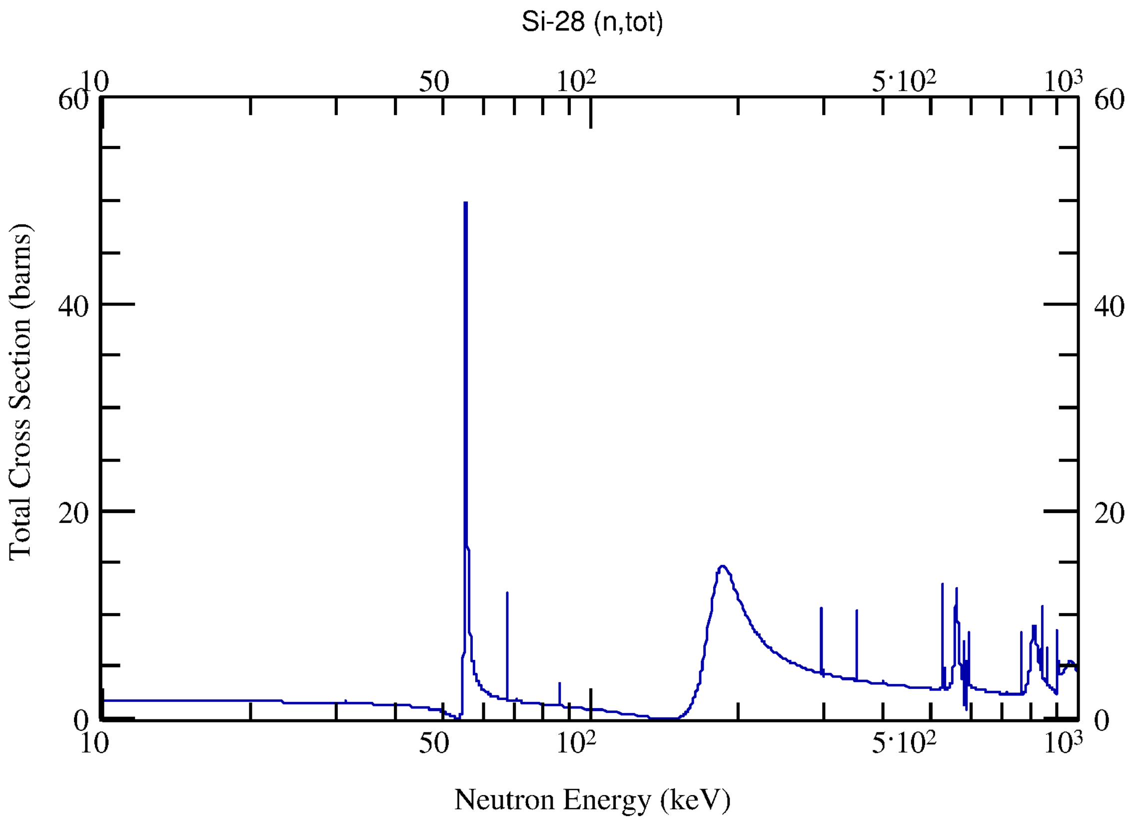


Figure 3-2. Neutron cross-section with Si as a function of neutron energy from 10 to 1000 eV. The peak seen at 55.7 keV is the resonance IMPACT took advantage of for both improved event statistics as well as a physical means of neutron energy selection. Figure taken from [51]

TUNL hosts a Tandem accelerator that produces a pulsed proton beam with energy of 1.88 MeV at 2.5 MHz. The beam pulses are registered by the beam pick up monitor with nanosecond resolution. This beam is incident upon a 100 nm thick LiF target that produces a neutron beam with two energies of 11 keV and 56 keV [52] with an energy spread of ∼1 keV. The neutron energy of 56 keV is selected to take advantage of the narrow neutron-Si resonance at 55.7 keV (seen in fig 3-2) to produce higher numbers of statistics as well as having a natural energy selector for the majority of the recoils. These produced neutrons are then collimated by high-density and borated polyethylene to the detector constraining their angle to within 4 degrees from the proton beam path. In addition to neutrons, the production of neutrons also produce gamma rays. A ~10 cm thick piece of lead is placed at the end of the collimator to reduce this background from hitting the HVeV detector.

The simulated event rates in the detector from particles generated in the LiF target are shown in Figure 3-3. The highest energy gamma ray is the most prominent gamma background that needed to be cut in our analysis. Fortunately the time it takes a scattered gamma ray to hit a photomultiplier tube is different than the time it takes a neutron to travel that distance so this background can be removed by a time of flight cut as discussed later in Section 3.5.

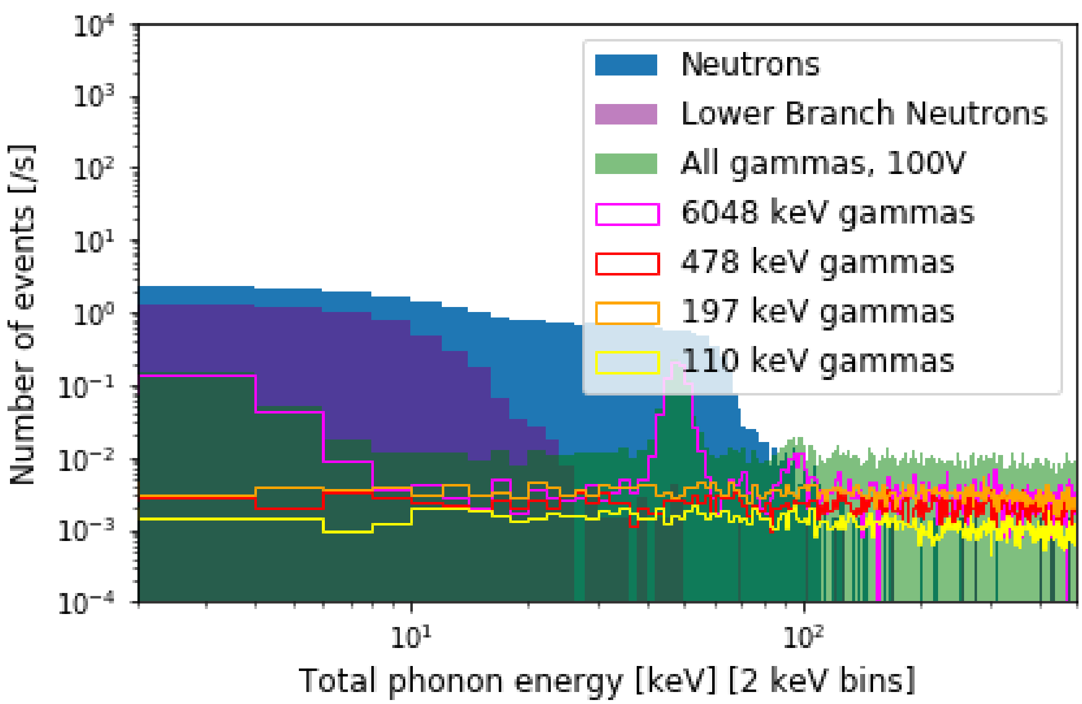


Figure 3-3. A simulated energy spectrum of event rates expected in the detector at 100 V NTL gain.

### 3.2.2 HVeV Detector

The HVeV detector is comprised of a 10x10x4 mm, 0.93g high purity Si chip instrumented with QETs on its top 10x10 mm face that have a superconducting transition temperature of 65

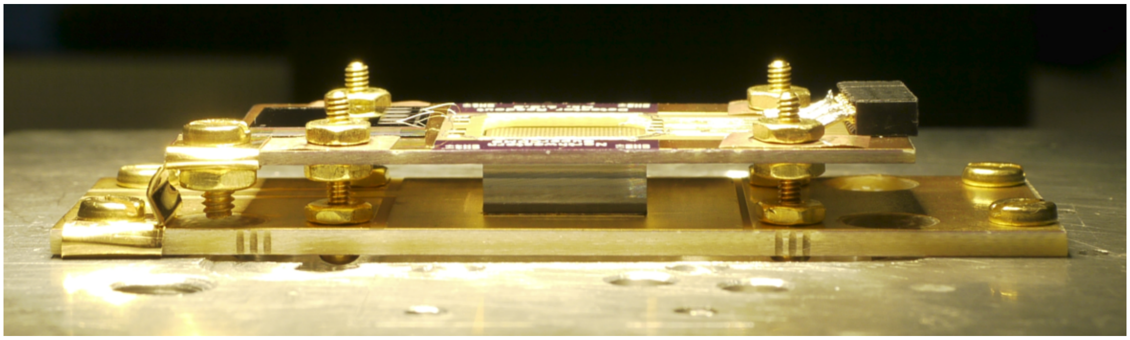

Figure 3-4. The sideview of the HVeV detector in its holder. The detector chip is pinned between two PCBs. A keen eye might notice the black strip on the left side of the top PCB. This was a secondary detector which is meant to used for background rejection but was not used in this run due to the operating temperature being too close to that detector's superconducting transition temperature

mK. The QETs are arranged with the NF-C detector mask that have TES lengths of 150 $\mu$m and Al fin lengths of 60 $\mu$m. This is the same detector mask that was utilized in HVeV Run 2 [53]. This detector mask has two channels, organized with an inner and outer channel to allow for a level of positional information of a given event. This detector mask is designed to have larger dynamic range than other detector masks, allowing for calibration across the entire energy calibration across the entire 100 eV - 108 keV total phonon energy range measure at IMPACT.

The bottom face of the detector chip is instrumented with Al in a parquet pattern to apply the NTL voltage bias across the crystal. This NTL voltage bias was operated at 0, 20, 100, and 180 V throughout the IMPACT measurement. The detector was sandwiched between two PCB boards (Fig. 3-4 and enclosed in a light tight copper case. The detector was operated at a bias current that placed the detector state at 30% of its transition curve to optimize dynamic range.

The HVeV detector was installed in a VeriCold Adiabatic Diamagnetic Refrigerator (ADR). This was stabilized to a temperature of 52 mK throughout the run. The ADR was temperature cycled to 4 mK daily. For daily low energy calibration, an optical fiber was ran from a 635 nm laser diode kept at room temperature. For higher energy calibration, radioactive $^{55}$Fe and $^{57}$Co sources were placed against the beryllium window on the side of the ADR several times throughout the run.

### 3.2.3 Liquid Scintillators / Photomultiplier Tubes

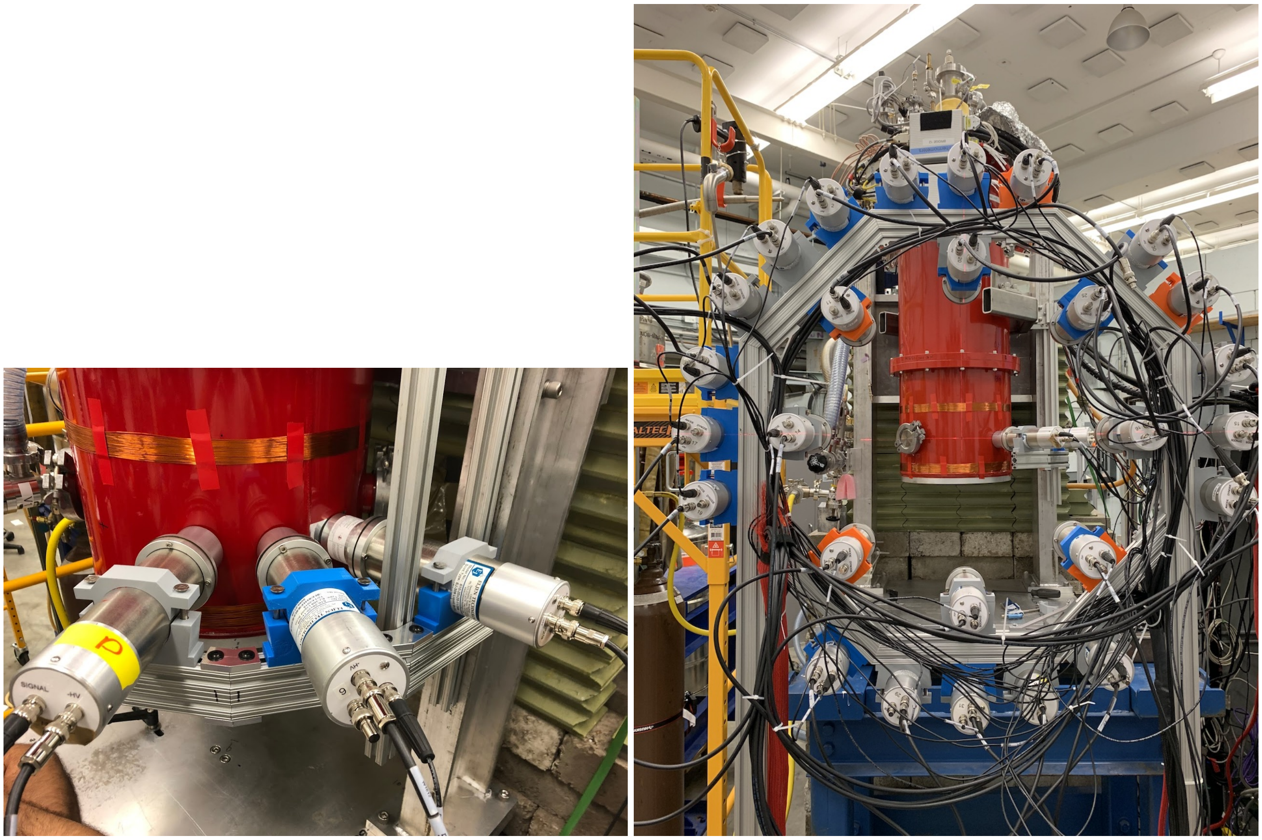

Figure 3-5. (Left) The three LW PMTs mounted in their position against the ADR. (Right) The ring of PMTs in position down stream from the neutron beam passing through the ADR and HVeV detector.

There were a total of 29 2 inch liquid scintillator units coupled to 2 inch PMTs, 3 placed against units placed against the ADR (referred to as Lone Wolf (LW) PMTs) at angles to collect neutrons with recoil energies deposited in the HVeV detector of 0.75, 2, and 3.9 keV. The remaining 26 were mounted in an array of two concentric rings, the outer containing 18 and the inner containing 8 PMTs. This array was placed at distances of 85.6 cm and 131.4 cm from the ADR at different segments of the run. This corresponds to the inner(outer) ring capturing 0.22(0.46) keV recoils at 85.6 cm and the inner(outer) capturing 0.1(0.22) keV recoils at 131.4 cm. These positions were chosen such that both distances capture a common recoil energy 56 keV neutron.

## 3.3 HVeV Detector Data Analysis

The analog signals produced from the HVeV detector were digitized with a custom Data Acquisition (DAQ) system which collected data continuously at a sampling rate of 1.51 MHz and uses an offline trigger to identify events and their timings. From these trigger times, slices of the data stream are taken to produce reduced 'event traces' that are small segments of time around each trigger. These event traces are the analysis windows for each trigger that a number of reduced quantities (RQs) are produced to determine the trigger characteristics, as well as if the trigger point matches well the expected signal response of the detector for the expected event energies.

### 3.3.1 Offline Triggering

Data in the HVeV detector was taken continuously on both channels. All data streams come in a one second long segment and therefore can have a number of events in a single recording. These data samples have to be reduced to shorter segments around each event for data analysis and producing the reduced quantities associated with each event. To do this, the two channel amplitudes was combined and then down-sampled by a factor of four. The second long traces were then convolved with an analytical form of the expected detector signal response shape as the difference of two exponentials with a rising time constant of 20 $\mu$s and a falling time constant of 80$\mu$s. This produced a 'filtered' trace that essentially produced an array of expected event amplitudes for an event that occurs at a given time sample.

The filter traces gives us an estimate of amplitudes in a given second long data sample. From this, we defined a trigger threshold of $\sim$50 eV, well below the analysis window considered by IMPACT. This threshold was used to determine the set of points in the data stream where the amplitude surpassed this value. For each triggering point, individual event cuts were made of 1024 samples before the trigger point and 3072 points after. This defines the analysis window for each event.

### 3.3.2 Event Magnitude Estimation

The recoil energy range of analysis in IMPACT spans from 100 eV to 109 keV. Over this large of range the detector response varies and due to saturation effects. To alleviate these issues and maintain reasonable energy estimation across this range, IMPACT uses a uniquely developed RQ which will be referred to as the IMPACT Matched Filter (IMF).

In previous data analyses it is typical to use an optimum filter (described later in detail in Section 4.3.2). This matched filtering scheme is used to estimate the an event's amplitude based on a fitting to a known signal shape (template) and is scaled by detector noise to minimize the effect of noise fluctuations on an amplitude estimate. Due to detector saturation, this scheme begins to fail above 6 keV. An alternative to this is to simply take the integral of the analysis window. The integral will have a varying value based on the extent of saturation and therefore give an energy estimate for the high energy events. However, by integrating over the large analysis window, one finds a loss in energy resolution due to the average difference between different levels of saturation washing out by the many sample estimate.

IMF used a selected region integration technique to maximize energy resolution while maintaining the ability to create energy estimates for saturated events. To do this the integral of points where there was high signal to noise ratio (SNR) was taken, which was empirically found to be regions where the signal is $>2\ \mu$A. The length of this region can vary based on the level of saturation. The region following this is where the detector is beginning to recover. In this region, an amplitude estimate is made by taking the inner product of the template with event trace. Then the integral of the amplitude scaled template is taken in these sub-2 $\mu$A regions. The sum of these two integral is taken to be the IMF and is used as an energy estimator across the entire analysis energy window.

In using this as an energy estimator, there are two effects taken into account that can bias this estimator value. The first is the drift in baseline gain through out the entire data collection run. To account for this, we apply a daily gain correction by scaling the IMF by a linear fitting factor produced by looking at peak positions of the of the daily laser calibration sets as well as the

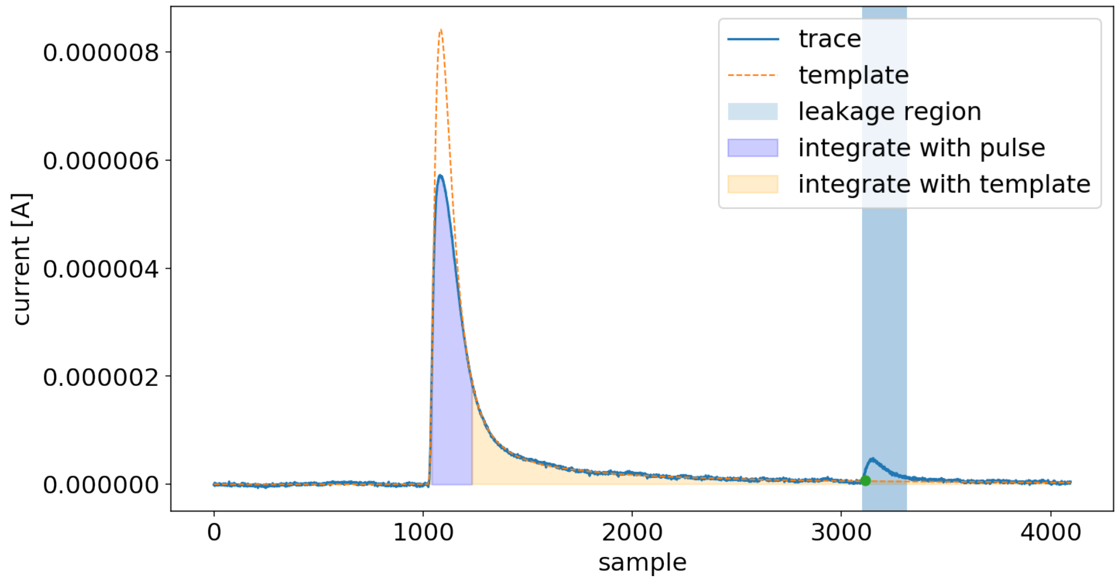


Figure 3-6. An example event trace and the construction of the IMF highlighted. A convenient aspect of this MF is the insensitivity to other events in the trace. By removing these segments of data before estimating the template amplitude, a more accurate estimation of the sub-peak integral can be made.

$^{57}$Co data and making it so the IMF is constant for a given baseline value. The second effect results from the existence of secondary events in the analysis window. This makes it so that the IMF is biased to a higher value due to the existence of multiple signals. To identify these situations, a Gaussian derivative filter is applied to each event trace. Rising edges will have large derivatives and are indicative of a secondary event in the window. For rising edges found greater than 50 samples from the trigger point, the region surrounding this secondary event is ignored in the calculation of template amplitude as to not bias the integral calculation in sub-2$\mu$A regions.

### 3.3.3 Energy Calibration

As mentioned in Section 3.2.2, IMPACT used several known energy sources for energy calibration and variation of detector response over the 100 eV to 109 keV analysis range. Specifically, the different calibration sets and purposes are as follows:

1. Low power laser at 100 V NTL bias taken daily for low energy calibration and estimation of day-to-day variations. Calibration range: 0-600 eV.

2. High power laser at 250 V NTL bias to extend laser calibration up to higher energies taken

on two days. Calibration range: 0.25-7.5 keV.

3. $^{55}$Fe with NTL bias varying from 0 to 70 V. Calibration range: 6 - 120 keV

4. $^{57}$Co at 0 V NTL bias. Calibration range: $\sim$100 keV

The combination of these different calibration sources is combined to produce an empirical function to scale from IMF to real energy.

In producing the energy calibration function, several data quality cuts and corrections were introduced to improve accuracy. The cuts used for energy calibration data are:

1. **Baseline Cut:** IMPACT analysis already includes a baseline correction for the energy estimator but this becomes less consistent at large variations in baseline. This cut removes any events with variation in baseline greater than 0.5 $\mu$A.

2. **Fridge Temperature Cut:** The ADR occasionally lost fridge temperature stability which in turn affects the gain of a given event. Events where the fridge temperature is measured to vary $>$0.05 mK from 52 mK are removed.

3. **High Voltage Correction:** The NTL voltage gain was set by hand-tuned knob and therefore not very precise. The voltage is recorded every second throughout data collection and the average for a given day is applied as the actual NTL gain for a given day. Daily drift in this measurement are $<$0.1% allowing for the daily average to suffice.

4. **Laser QET Absorption Correction:** Some photons are absorbed by the TES directly and do not produce an NTL gain as a result. This effect causes a flat shift in measured laser energy and is a function of the applied laser power. By looking at the zeroth peak of the laser data this shift is quantified and added to the energy estimation of each peak.

### 3.3.4 Laser Calibration

The laser calibration data is used for both energy calibration in the range 0-7.5 keV and calculation of the daily gain correction. The high power data produces more electron-hole pairs on average and is taken at a higher NTL voltage. It therefore extends to much higher calibration

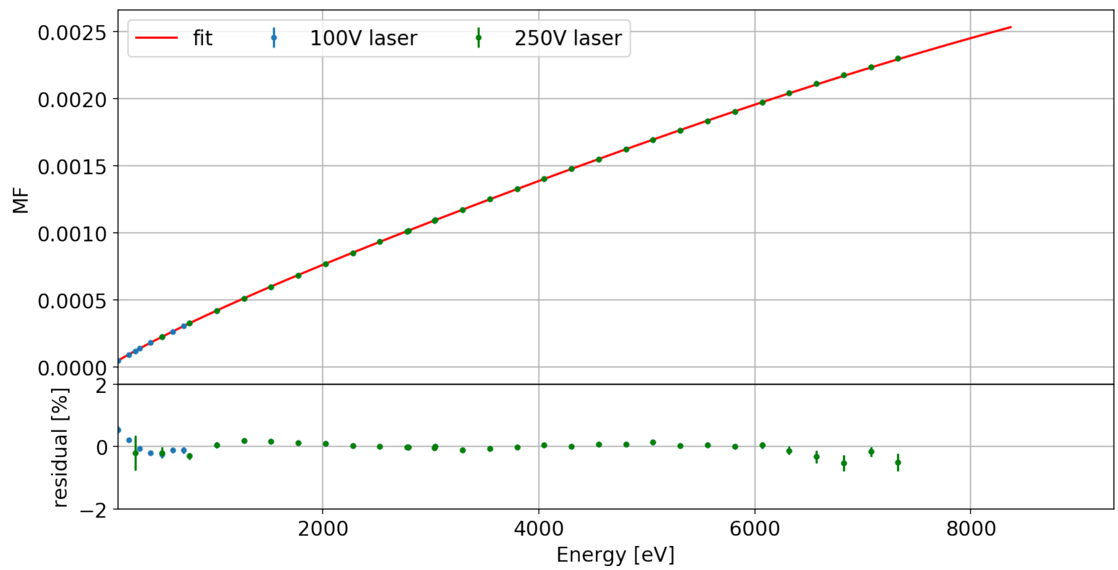


Figure 3-7. The resulting overall laser calibration function using both 100 V and 250 V laser data.

energies. At higher energies, resolution gets worse and peak widths get wider due to detector crystal effects like charge trapping and impact ionization[1]. To enhance the SNR of the peaks with lower statistics, the overall Gaussian shape of the laser spectrum is subtracted off in this case. Gaussian distributions are then to fit to the peaks in the residual spectrum to identify each peak position. For the low power data each peak is fit directly without any attempt to remove the background spectrum as the peaks at this energy already have reasonable SNR. The average position across the entire run for each peak is then taken. The results of these two types of laser data are combined and fit to a fourth order polynomial to produce the laser calibration function (Figure 3-7).

Comparisons between the daily laser calibrations set show inconsistency in IMF depending on the day. The data for each day is corrected for this effect by a daily gain correction. This gain correct is taken to be the ratio of the calibrated energy of each daily low energy laser set to the actual energy each peak should have. This correction reduces the variation in peak energy from 10% to approximately 1%. This correction is calculated with laser deposition energies less than 1 keV but was shown to remain consistent at higher energies. It is plausible to assume this makes

1 These effects are described in depth in Section 4.6.2

sense as the variation in gain on the day-to-day is a function of detector conditions and not the energy of the given events.

### 3.3.5 Radioactive Source and Combined Calibration

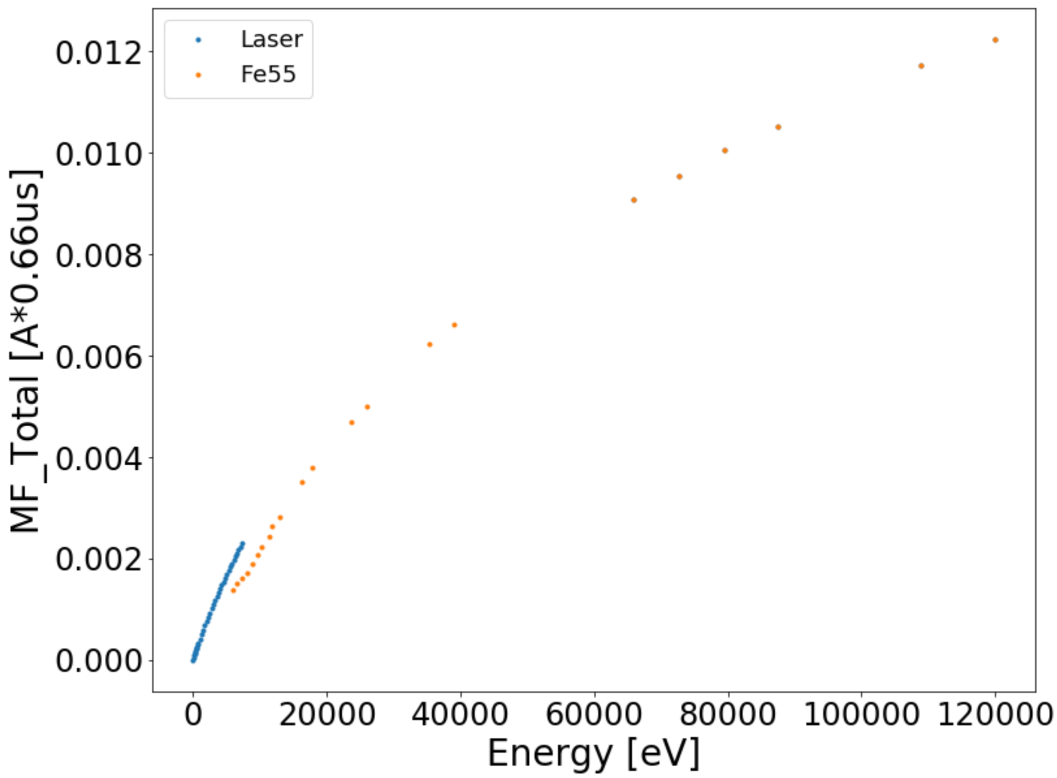


Figure 3-8. A combined plot of all laser data and $^{55}$Fe data. Deviations at low total phonon energies are thought to be due to the small penetration depth of X-rays causing absorption very near the QETs.

The two radioactive sources used in the IMPACT measurement were $^{55}$Fe and $^{57}$Co which have dominant emission lines at 6/6.5 keV and 122/136 keV respectively. The $^{55}$Fe source was used with with NTL gains ranging from 0 V to 70 V and the $^{57}$Co was only taken at 0 V. The IMF spectral peaks for these data sets were fit directly and the $^{55}$Fe calibration points are plotted alongside the laser calibration points in Figure 3-8. We saw a large deviation in the calibration for the low NTL gain data sets. This is thought to be due to local saturation effects due to the x-rays produced only having a penetration depth of several micrometers. This means that a significant fraction of these x-rays generate prompt phonons very close to the QETs and can have a different phonon collection efficiency and pulse shape. For this reason it was decided to only consider $^{55}$Fe data with NTL ≥40 V. With a significant NTL gain, the NTL phonons will dominate over prompt phonons making this local saturation effect less apparent. Further issue was seen when

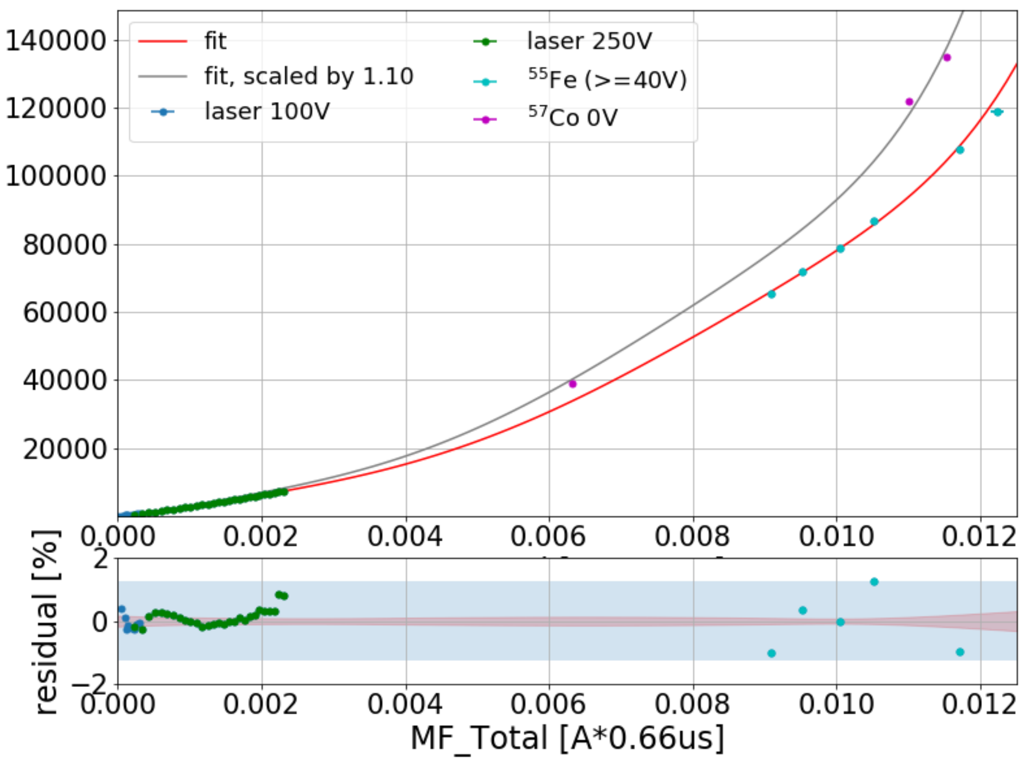


Figure 3-9. The final calibration function used across the entire analysis range. The red fit excludes the $^{57}$Co data and is used for data above 100 V NTL bias. The grey curve is found empirically by scaling the red fit by 1.10 and is used for 0 V data.

considering the $^{57}$Co data as the calibration points generated from this did not follow the trend of the $^{55}$Fe data. This is seen in Figure 3-11. The three $^{57}$Co points correspond to the two x-ray peaks and the 39 keV Compton edge. The red curve was the fit to the chosen $^{55}$Fe data and the laser data. The grey curve shown is a simple scaling of the red curve by a factor of 1/1.10. The hypothesis for this difference is that the prompt phonons have different collection efficiencies compared to NTL phonons and therefore find a different detector response in the two operating points of 0 V and HV. For this reason the red curve was used for calibrations of data sets with NTL voltages ≥100 V and the gray was used for 0 V data.

## 3.4 PMT Data Analysis

The important components of the PMT analysis were determining if a given event had a reasonable response energy and the timing of the event. This is simply because the PMTs were used to only identify when neutrons scattering in the HVeV detector ended up in a PMT. The energy estimator used for PMT analysis was the sum of the 5 samples before the PMT trigger and 7 samples after. Energy calibration data was taken daily by looking at the 477 keV Compton edge of a $^{137}$Cs source. As this calibration was only performed with one data point, the response was assumed to be linear and pass through the origin such that zero integral meant zero energy. To this roughly calibrated energy spectrum a Gaussian fit was applied and 80% of this peak energy was taken to be the energy threshold for events to be considered in the analysis.

Several data quality cuts were also applied to the PMT data. To summarize these:

1. **Saturated event cut:** Saturated events in the PMT corresponds to energies on the MeV scale, well outside the range that a 56 keV neutron could produce. Therefore all such events were removed.

2. **Strong Pile-up Cut:** The PMTs have two timing RQs, one measuring from the beginning of the trace and one from the end. By confirming that the difference between these two RQs is less than 2.5 ns, one can confirm that both RQs are finding the same trigger point, or same event. In addition, if both RQs return a negative number that means no event was found. Therefore if the difference is too great or both RQs return a negative number then the event was removed.

3. **Relaxed Pile-up Cut:** Some traces with pile-up can be saved. A neutron event trigger is expected to be at 120 ns in the trace. This cut confirms that the trigger at 120 is not a follow up scintillation of a high energy gamma that hit the detector previously, as well are confirms that the triggered event occurs at sample 120. This cut was used in cases where the strong pile-up cut removed too much statistics for the coincidence analysis to be performed.

4. **Comparison of Max Peak Value to Integral:** This cut compares the integral described

early in the section to the maximum value measured for an event. Events that occur and drop in signal too quickly aren't likely to be liquid scintillator events. Thereby confirming that the integral is enough of a factor larger than the max bin value confirms that the signal lasted the expected amount of time. On the other hand, sometimes the peak maximum is too small compared to the integral. The source of these events isn't well understood and they are also removed.

## 3.5 Coincidence and Timing Analysis

The timings seen at the HVeV detector and PMTs ares the vital component to correlating events between the two as well as identifying events as neutrons. This was a considerable task as the HVeV detector and PMTs were running two separate DAQs and were connected to two different computers. These DAQs also had two very different sampling frequencies of 1.515 MHz and 250 MHz for the HVeV detector and PMTs respectively. Synchronization of these two systems was done by comparing the available timestamps: the computer's timestamp, the PMT's timestamp, and the HVeV timestamp, as well as using a Time Syncing Pulse (TSP) which was generated by an external function generator that pulsed a signal once every minute and was connected to both DAQs.

To achieve this synchronization, first the computer timestamp was used in combination with each DAQ timestamp and DAQ clock cycle to determine the timing of the TSP. Then the smallest difference between these two timing was found and the HVeV clock was corrected for this difference. Then the variance in clock speed between the two systems is calculated and a PMT precision timestamp of each HVeV event. Then PMT and HVeV events within 100 $\mu$s of each other were labeled as coincident. This is certainly too large of a window for these to truly be the same neutron, but from this a coincidence cut was developed.

Before looking at the coincidence cut, the data selection for the coincidence analysis must be defined. For the HVeV detector an asymmetric cut of any baseline value outside of the range (-0.1,1) $\mu$A WAs removed, and pile-up events were removed if a given event trace has more than two additional events. The PMT data applied the same cuts as described in Section 3.4 in addition to an energy specific cut removing any events outside the range (1.5,10) keV and a cut specific to PMT 14 requiring energies greater than 4 keV.

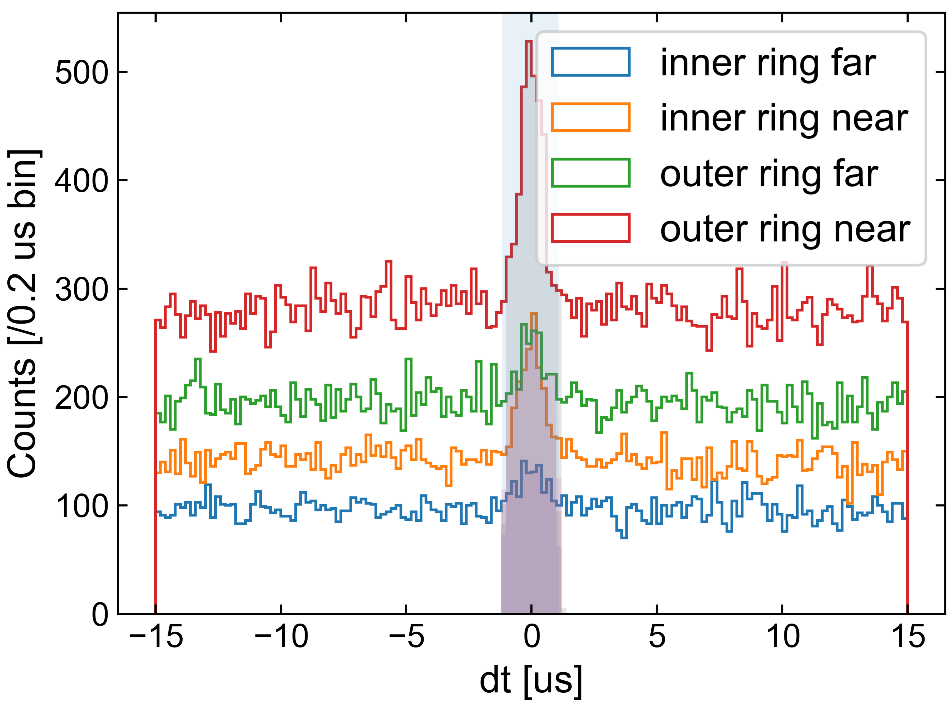


Figure 3-10. The corrected dt spectrum for all the ring detectors.

The coincidence cut is made by looking for a peak in dt, the timing difference between an HVeV event and a PMT event. This dt Reduced RQ (RRQ) has to be corrected for an energy dependence introduced primarily from saturation in the HVeV detector. By taking small energy slices an energy dependent function of dt was generated and corrected such that the peak in dt for each energy is centered at zero for the LW PMTs. This variation was further corrected for the ring PMTs by fitting this corrected dt distribution to a Gaussian plus a flat background and then subtracting off the mean of this fit such that the peak for dt with these PMTs also lie at zero. This extra step is required for the ring PMTs because of the time it takes for the neutrons to reach the ring array. Finally a Gaussian fit was applied to all the data to find the variance to this peak and the final window of vents determined as coincident is set at three times the variance.

### 3.6 Ionization Yield

The final ionization yield fit is shown in Figure 3-11. This fit was made with an empirically determined power law function

$$Y(E_r) = Y_{10\text{keV}} \left( \frac{E_r}{10000} \right)^B . \tag{3-4}$$

This was constrained to match the value for the Lindhard model at 10 keV ($Y_{10\text{keV}}$). There is some variance from measurements made with a photo-neutron source [54] and a more recent result using silicon neutron capture [55]. A key result however is the lack of any sign of an ionization production threshold down to the 100 eV range. This is key for SuperCDMS and other experiments for low energy rare event searches in semiconductors.

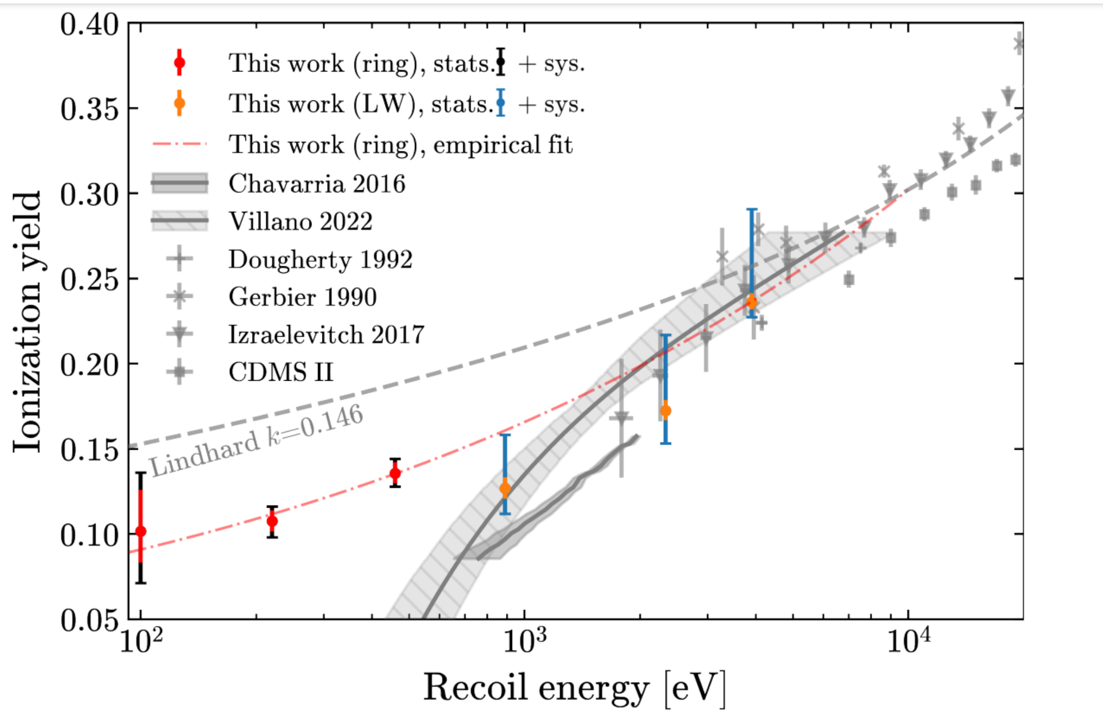


Figure 3-11. The final ionization yield results shown in red for the ring detectors and orange for LW detectors. This is plotted against other previous yield measurements. The empirical fit to the ring detector measurements is shown as the red dashed line.

# CHAPTER 4
# HVEV RUN 3

## 4.1 HVeV Run 3 Goals

HVeV Run 3 is the third electron-recoil and absorption dark-matter search using the SuperCDMS HVeV detector design. The first HVeV run showed the power of the cryogenic calorimeters for the detection of sub-GeV dark matter by setting a world-leading limit in electron-recoil dark matter searches. The second run implemented the second-generation detector-chip design, which improved the energy resolution from 14 eV to 3 eV. Run 2 also included charge trapping and impact ionization (CT and II) within the limit-setting signal models. Run 2 saw success in improving detector performance, but the limit did not improve because the underlying background was the same.

It turns out that low energy background events with energies less than one electron-hole pair seen in Run 1 and 2 are a major barrier towards improved sensitivity. Studying these events seen in Run 2 we find a type of event in our detector characterized by a first pulse of variable amplitude followed by several secondary signals with energies typical of 1 electron-hole pair . We will often refer to events of this nature as ”burst events”. The behavior of these events was studied and characterized both with and without the Neganov-Trofimov-Luke (NTL) amplification. The resulting hypothesis is that these events are due to scintillation from the PCB holder clamping the detectors in place. This run allowed us to test if the main background of the HVeV detectors is internal or external to the detector chips, for example spontaneous electron-hole pair production or scintillation off the detector housing respectively, using coincidences between detectors. This run's experiment site is located 107 meters underground compared to the previous runs that occurred at the surface. In addition to external lead shielding, these two sources of reduction from atmospheric and local environmental signals help narrow down the potential sources of these background events. This run's payload includes four separate silicon detector chips, each the same dimensions and mass as the detectors in Run 1 and 2. These detector chips were placed in pairs on two sides of two separate detector holders with all four along the same central axis. This allows for discrimination of events based on close time occurrence of signals seen in multiple detectors creating a signal veto for events of this type, introducing a very powerful live-time cut not previously possible in Run 1 or 2. Additionally, Run 3 analysis implements several improvements including better pile-up event[1] identification through the delta chi-square optimum filter data quality cut and improved CT and II modeling. It is the goal of Run 3 to achieve improved sensitivity through better identification and removal of these troublesome background signals.

This chapter presents the analysis work produced by the SuperCDMS HVeV Run 3 analysis team: Taylor Aralis, Derek Sincavage, Alex Zaytsev, and myself. In addition to all the hours of work put in by myself and others in the SuperCDMS collaboration at the NEXUS facility.

## 4.2 Experimental Setup

HVeV Run 3 data acquisition occurred from December 2020 to February 2021, during NEXUS run 7. The experiment was hosted at the Northwestern EXperimental Underground Site (NEXUS) located at Fermi National Accelerator Laboratory in Batavia, Illinois. This facility is located 107 m underground equating to 300m water equivalent overburden and employs lead shielding both internal to the refrigeration system as well external shielding covering most of the local environment's line of sight to the detector payload. NEXUS uses a CryoConcepts dilution refrigeration system which we regulated above base temperature to 10.5 mK. This system requires no temperature cycling, allowing for uninterrupted, consistent data collection throughout the run.

The detector payload consisted of four 10 x 10 x 4 $mm^3$ (0.93 g) silicon chips. These silicon crystals are instrumented with two QET channels which cover the top surface of the detector. The bottom surface has a 5% coverage parquet patterned aluminum grid used to apply the NTL bias at 100V throughout the entire run. Each chip used a different instrumentation mask including: the NF-C, NF-F, NF-H masks designed in the second generation of HVeV detector masks and the Run 1 detector mask (but a different chip than Run 1). Compared to the R1 mask, NF-C,H,F masks improve upon energy resolution, dynamic range, and sensitivity to fiducial information. NF-C mask maximizes dynamic range with limited loss of energy resolution, the NF-H/NF-F masks have better positional resolution and ensure phonon fall-time is comparable to

1 Pile-up events are any events where one or more additional events lie in the analysis window for a given event.

TES fall-time (for RF/real event differentiation). Each chip was mounted by sandwiching it between two printed circuit boards (PCBs) and attached to the front or back of one of two L-brackets with cut outs such that each instrumented face is vertical.

This is all installed in a copper cavity fixed to the mixing chamber stage of the fridge. In order to improve the light tightness of the copper cavity, the electrical and fiber feed-through were epoxied with eccosorb and the sides of the mating surfaces were taped with copper tape. At the bottom of the cavity, a polished optical fiber is fixed in-between the two L-brackets and connects to a laser diode located at room temperature. The photons coming from the laser diode are used as signal proxy for the analysis development. The fiber shines light in the cavity and is not directed to any of the detectors specifically. Given the mounting geometry of the 4 detectors, it is more likely that the photons will hit the side of the detectors, but there is not a clean line of sight between the optical fiber and the detectors. Photons from this fiber are used for energy calibration of signals in the detectors. Eight SQUIDs are used for the read-out of 4 detectors (each detector using 2 channels for the inner and the outer sensor). The SQUIDs are fixed to the bottom part of the 1 K shield and reside below the payload. These signals are then digitized and stored by the SuperCDMS Detector Control and Readout Card (DCRC) which is plugged directly on the cryostat feed-through at room temperature.

Though the original intension was to use all four detector chips as part of the run's data set, the difference between detector performance between the NF-C detector masked chip and the other remaining three was significant enough to instead only consider the NF-C detector chip for the source of our dark matter search data and only consider the other detector chips for data cut considerations. Moreover, the NF-F detector was not operational, which made the NF-C detector to be the only one having other operational detectors on both sides, which gives a better potential to subtract external backgrounds by utilizing anti-coincidence cuts. Including other detectors into the final spectrum would not improve our reach, but on the contrary would limit it, due to the poorer potential of the anti-coincidence cuts in these detectors. Throughout this chapter each detector chip is referred to by their detector mask (NF-C, NF-H, NF-F, R1), and in cases where not explicitly specified any science data should be considered as only sourced from the NF-C detector chip.

## 4.3 Data Processing

### 4.3.1 Triggering

In previous runs, data was collected continuously on the two active channels for a single chip. In Run 3, four detectors with two channels each was too much for the DCRC to output (maximum 4 MB/s) so instead only 50% of live-time is recorded. The data was sampled such that random 0.5s long data streams (known as MIDAS traces) were taken randomly at a 1 Hz rate, such that no 0.5s interval overlapped with another. This 0.5s sample recorded data on all active channels.

Following collection of these MIDAS traces, each is analyzed offline with a set of code designed specifically for HVeV Run 3. Each MIDAS trace can hold any number of individual events depending on the activity in the channel or detector at the time. The act of identifying and separating each of these events is known as triggering. Triggering in a given channel occurs when the measured amplitude in a channel surpasses a certain threshold, marking a trigger point. This trigger point was set at approximately 25 eV for NF-C and NF-H detector chips and 50 eV for the R1 detector chip. These points were set such that they are well below the first electron-hole pair peak ( 100 eV at 100V NTL bias) as well as low enough to include sub-eh events that only receive partial NTL amplification for a number of reasons. The threshold is set much higher for R1 than NF-C/NF-H because the measured energy resolution of each are approximately 10eV and 3 eV respectively, placing the threshold for each well outside the possibility for triggering on a noise fluctuation.

Before measuring each trigger point, each MIDAS trace is filtered with a Gaussian derivative filtering kernel which smooths away high frequency noise and allows for better identification of triggering points, as well as any close lying triggers that lie inside the analysis window for a given event. This is different from previous HVeV runs, as well as the trigger described in IMPACT, which used optimum filtering to produce the filtered traces that are triggered. This decision was made because it is seen in the case of triggering upon an optimum filtered trace there are some times trigger artifacts introduced in filtering of saturated traces or traces with high levels of pile-up events.

### 4.3.2 Optimum Filtering

Optimum filtering, also known as matched filtering, is a signal processing technique used to detect and extract signals of interest from noisy data. Matched filtering maximizes the signal-to-noise ratio (SNR) by convolving the received data with a noise weighted template or reference signal that closely matches the expected characteristics of the signal being sought. The template waveform is typically derived from the expected shape, duration, and other properties of the signal. The noise of the detector is measured by randomly selecting traces from the data segment and using reduced quantities such as mean, slope, and standard deviation of the trace to identify samples with no significant signal present within it.

Both the template ($s$) and noise ($J$) are then Fourier transformed to frequency space and compared against a given event trace ($v$) producing a chi-square reduced quantity:

$$\chi^2 = \int_{-\infty}^{\infty} \frac{|v(f) - As(f)|^2}{J(f)} df \tag{4-1}$$

where A is the amplitude of the template necessary to minimize this noise weighted difference between the signal and template over all frequencies. Performing a minimization of the $\chi^2$ with respects to A shows that it is useful to define a so called optimum filter as

$$\phi(f) = \frac{s^*(f)}{J(f)}. \tag{4-2}$$

Normalizing the filter gives a very simple form for the amplitude estimation of each signal of the form

$$A = \int_{-\infty}^{\infty} \phi'(f) v(f) df. \tag{4-3}$$

From this amplitude estimation in current one can calibrate these to an energy scale using injected known energy events.

### 4.3.3 Laser Data Selection

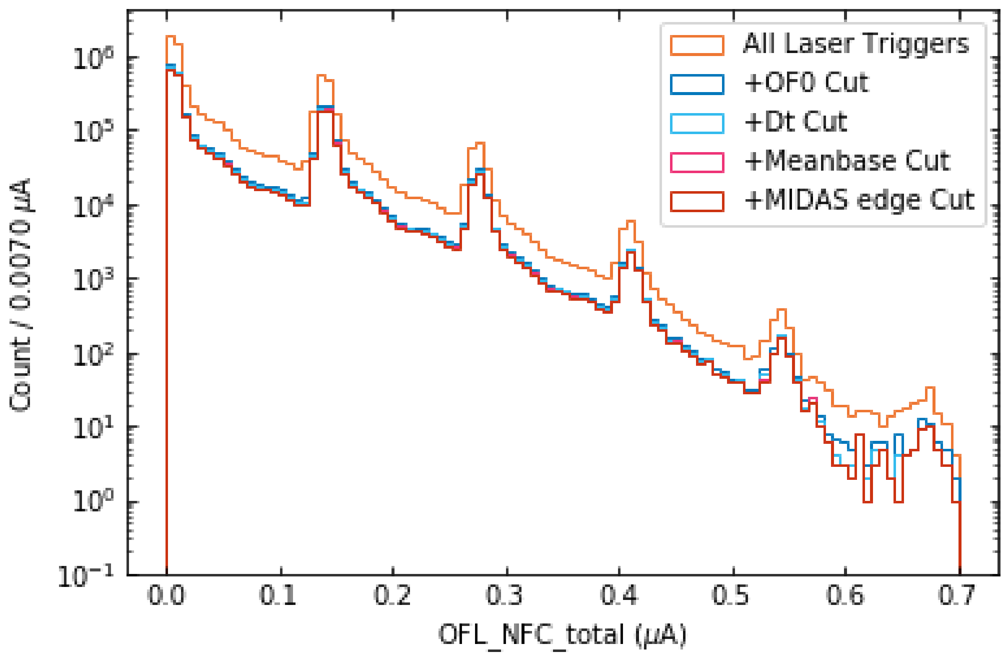


Figure 4-1. The OFL spectrum from laser data before and after all the laser specific live-time cuts. This greatly improved the spectral shape near the electron-hole pair peaks.

Laser data sets were taken throughout the run to serve as a proxy for dark-matter response in our detectors and were used for determining the data quality cuts and energy calibration to be applied to Run 3 science data. Laser events were generated using a laser diode and sent to the payload cavity using a fiber optic. The diode produced photons with wavelength of 635±5 nm (1.95±0.015 eV). Run 3 saw particular issue with our in-run laser data due to the configuration of the laser in the detector cavity. As this run included four detector chips on two detector holders, the laser was not positioned particularly at a detector, and shone at an angle far from the normal direction of the instrumented planes of the detector chips. This differs from previous HVeV runs where there was only one detector chip with the laser aimed directly at the instrumented face.

The positioning of the laser in Run 3 likely caused a large portion of laser events to be sidewall events and made laser peaks in our energy spectrum far from Gaussian. We found we could reduce this effect by reducing the laser lambda (laser power) towards the end of the run, and decided to do one extremely long laser run (24 hours) with a high burst rate (200 Hz) at a lower power setting to ensure enough statistics on the 4th peak (the highest energy peak used in the limit setting) despite the time constraints of the cryogenic run. This sample is the dominant statistic used for energy calibration discussed in section 4.5.2 and completely defines the data quality cuts discussed in section 4.4.2

Though this long laser sample improved the issue of our spectral shape, the burst rate is high enough that it induces an intrinsic pile-up of TTL events in our analysis window for each event (5 ms spacing between TTL triggers over a  13ms analysis window). However, since this laser set has high statistics and a low average number of photons emitted by the laser, we can find enough laser events with the previous and next laser events are not seen in a given event trace. We list below the cuts we applied to the laser data sets to define the sample of laser events used throughout this analysis (calibration, data-quality cut efficiency calculation and detector response studies). All the listed cuts are considered live-time cuts:

OF0 cut: This cut checks that the OF0 amplitudes of the previous and following TTL triggers are below a threshold of 5 sigma of a channel's baseline resolution to ensure that these events are not producing visible signals in the detector for the 200 Hz laser sample. This 5 sigma cut is lower amplitude ( 15 eV) than our triggering threshold ( 25 eV) and is measured by a fit to the OF template therefore removing events with these previous and/or post TTL signals with higher efficiency than the dt cut described below. To reiterate, the point of this cut is to remove events where the previous and/or post TTL event is registered in the detector because the TTL signal rate is 5 ms and the analysis window (event trace length) of each event is 13 ms. Therefore we need to find events without the previous and next TTL trigger to have a good laser sample to serve as our DM signal proxy for setting both calibration and data quality cuts of our science data.

Dt cut: This cut removes the laser events (triggered by a TTL trigger) whose time distance to the next Gaussian-filter-triggered events (so either a science data event or a laser event) is less than 7 ms. A similar delta-time cut was applied in the science data (see Section 5.1.4), however we use a tighter time window for the laser data than for the science data to avoid removing too many laser events(dt-laser >7 ms and dt-science >20 ms). This choice was dictated by the higher Gaussian-filter trigger rate in the laser events which includes both the laser events above threshold and the science data triggers. Note the laser TTL rate corresponds to 200 Hz. The 7 ms second window ensures there are no triggers within the analysis window window (+- 6.5 ms) and that the tail of events occurring just before the analysis window are not biasing the laser reconstruction.

Meanbase cut: A mean baseline cut to ensure the detector baseline is stable on each MIDAS trace. This is applied in the same way as the mean baseline cut is applied to science data.

MIDAS edge cut: A trigger time cut removing any events too close to the edge of the MIDAS trace such that any pile-up in the event's pre (or post) trigger parts of the trace selection would not be triggered on. For the 200 Hz laser data set there is always such a TTL event at the beginning and ends of the MIDAS trace.

## 4.4 Data Selection

### 4.4.1 Live-time Cuts

Run 3 included a number of live-time cuts to remove periods of data where the detector is either in a non-ideal state or periods where background signals are polluting the data stream.

#### 4.4.1.1 Intersecting MIDAS traces cut

The DCRC was designed to create half a second long non-overlapping traces. However, a small number of traces were found to still be overlapping in time. This cut was developed based on the trigger time of the traces and removed events where the times of traces overlapped by the length of the event trace.

#### 4.4.1.2 Mean baseline cut

Stability of the baseline current signal is a good indicator of the stability of the detector. When high energy events occur in the detector this can cause large saturating signals that lead to inaccuracies in event reconstruction of events that occur during the recovery from these saturating signals.

The mean baseline cut for the Run 3 is calculated on each half-second long MIDAS trace by taking the average baseline of 5 randomly triggered event traces within the MIDAS trace. The baseline of an event trace is defined as the first 4086 samples of the event trace, or half the event trace minus 10 samples as to be certain this baseline calculation does not include any portion of a triggered event. For each series a Gaussian fit is made to the distribution of average mean baselines for each MIDAS trace and any that lie more than 3-sigma away from the distribution center is removed. This cut removes 6% of the live-time when applied without any other cuts.

The cut is produced in this way as to find regions of time where the detector is deviating from normal operating state for any given reason, making this a live-time cut. If the cut were defined based on a triggered event trace's deviation from the average this instead qualifies as a data quality cut and would be included in the final analysis exposure calculations.

#### 4.4.1.3 Temperature cut

The temperature of the dilution refrigeration is very stable and maintained a measured temperature deviation of less than 0.1 mK from the set value of 10.5 mK for all but two series throughout the run. These series saw sharp temperature jumps due to a reset of the software controlling the thermometer which regulates the mixing chamber temperature. These series were removed resulting in a 4.4% cut from the total live-time.

#### 4.4.1.4 Coincidence cut

The coincidence cut takes advantage of Run 3 being the first HVeV run to include more than one detector. As mentioned in section 4.1, HVeV run 2 noted a particular type of pile-up event which was characterized by a multiple electron-hole pair event followed by a burst of single electron-hole pair events which we've denoted as burst events. These events can be identified by looking for multiple triggers in a small time window on one detector, but the addition of multiple detectors allows for better identification of environmental backgrounds causing triggers in multiple detectors and thereby remove these periods of live-time.

The coincidence cut is developed by looking at the dt between the signal detector, NF-C, and the veto detectors: NF-H, R1, and NF-C itself. In this way, the coincidence cut refers to a simpler one detector dt cut as described in section 4.3.3 as well as correlations in time of signals between two different detectors. Figure 4-2 shows the correlations of NF-C with both NF-H and

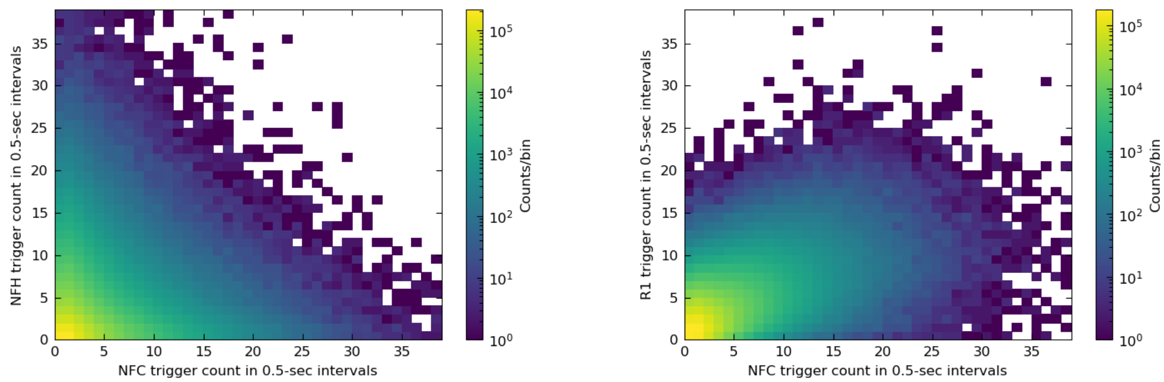


Figure 4-2. Two dimensional histograms showing the number of triggers in a given MIDAS trace for NF-C vs NFH(R1) on the left(right).

R1 detectors. There is a notable correlation between NF-C and R1 which is likely due to both detectors being on the same detector bracket and physically closest to each other. Figure 4-3 shows this correlation between triggers in NF-C and any detector where the peak near 0 dt deviates from what would expect that random and independent events would produce. The largest correlations are again seen between NF-C and R1, as well as overabundance of close triggers within NF-C itself indicative of burst events.

From this analysis it was decided to remove 20 ms of live-time before and after any trigger which had another trigger within this window in the same detector or another. This window was decided by finding the interval that maximized the amount of live-time remaining for relative reduction of event rate. All triggers were considered in this cut for NF-C and NF-H detectors while an amplitude cut of 0.01 $\mu$A was applied to R1 triggers as it was a much noisier detector compared to the former two. When this cut is applied to the full science data set 22.9% of the live-time remains.

### 4.4.2 Data Quality Cuts

The data quality cuts both deal with using the chi-square of the signal event's fit to the optimum filter. These remove signals whose shape do not match the expected shape of a single energy deposition within the crystal volume.

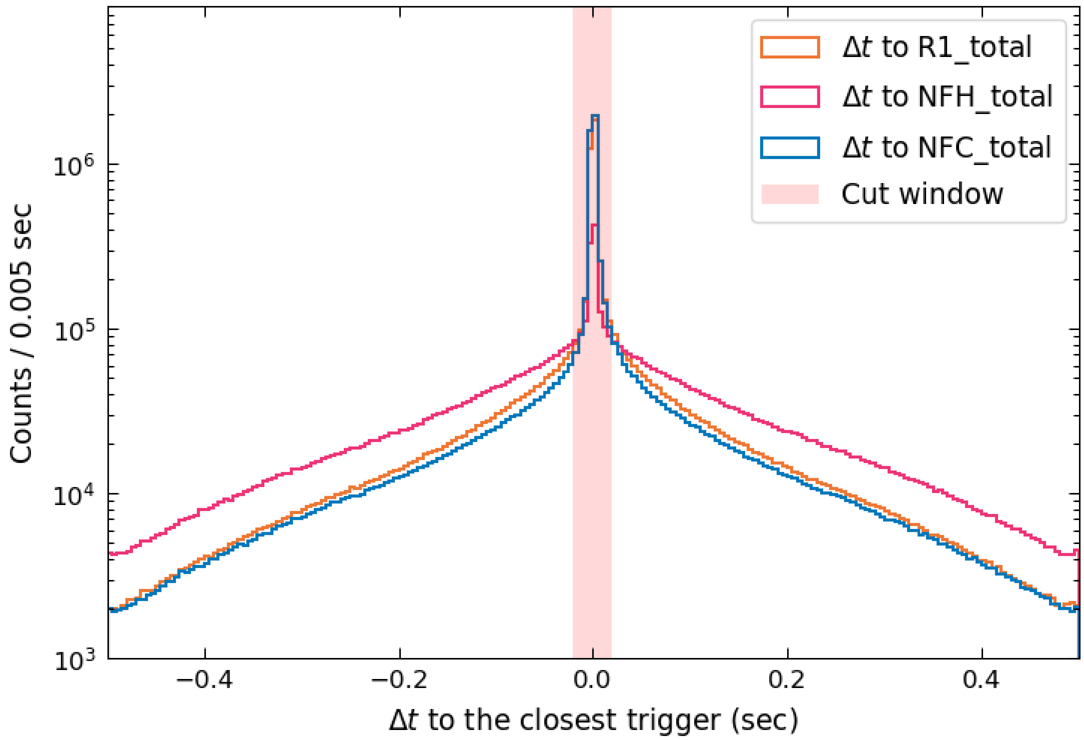


Figure 4-3. The dt between the closet triggers seen in any detector and triggers seen in NF-C. The peaks at close to zero dt are where the spectrums deviate from what would be in random coincidences. The peaks are strongest in NF-C to NF-C and NF-C to R1 due to pile-up events in NF-C and R1 being in the detector holder respectively.

#### 4.4.2.1 Chi-square Cut

The OF chi-square cut is based on the goodness of fit between a given signal event and the optimum filter template in the frequency domain. In this case, we use the OFL reduced quantity, an optimum filter fit that picks the best time delay within ±15 samples from the event trigger point. This small time delay range was set to improve the likelihood that the optimum filter template is fit to the signal that generated a given trigger. In addition, our chi-square reduced quantity uses a low pass filter at 30 kHz to remove high frequency noise.

This cut was calculated on the long laser data set (R3 Laser Data Sample) taken during the run which also established an energy dependence in our signal response seen here (as well as other part of the analysis) that should be accounted for. The cut was defined by the following procedure:

1. Make energy selections around each electron-hole pair peak
2. Make a Gaussian fit to each peak
3. Select all events within 3-sigma from the mean
4. For each energy selection, calculate the cumulative data distribution (cumulative distribution function produced from the data)
5. Find the 95% point for each distribution (one-sided interval)
6. Fit these points as a function of energy to the form $y(E) = AE^n + B$

The resulting functional fit defines the chi-square cut used throughout the analysis. The cut was defined on the first half of the curated long laser data sample described in Section 4.3.3. The cut efficiency is defined on the second half of the curated laser sample by the ratio of (curated laser events after chi-square cut)/(total curated laser events) in that half. Error in the efficiency is measured using Poissonian error in each histogram which then is propagated to the cut efficiency through a Bayesian statistical method defined by pyROOT, a python wrapper package for the ROOT language.

#### 4.4.2.2 Chi-square Results

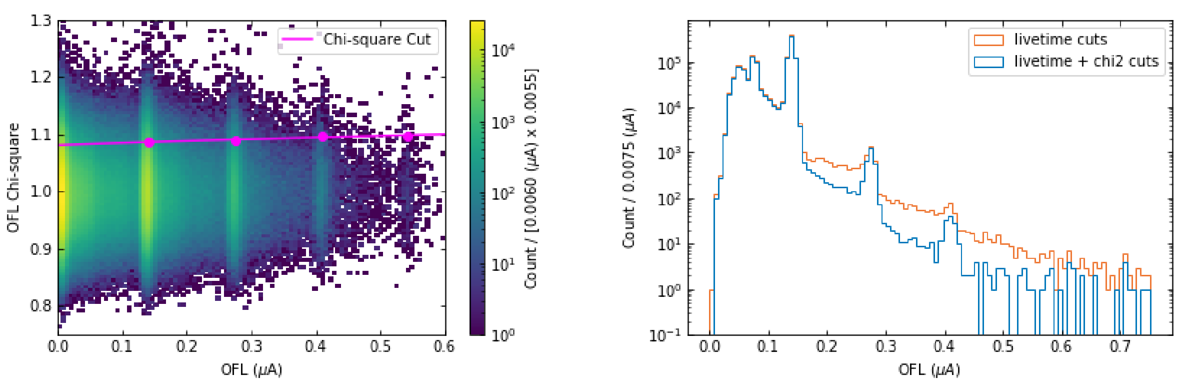


Figure 4-4. (Left) OFL vs. OFL chi-square 2-D histogram of laser data with the chi-square cut plotted over.(Right) The OFL spectrum of science data plotted with and without the chi-square cut.

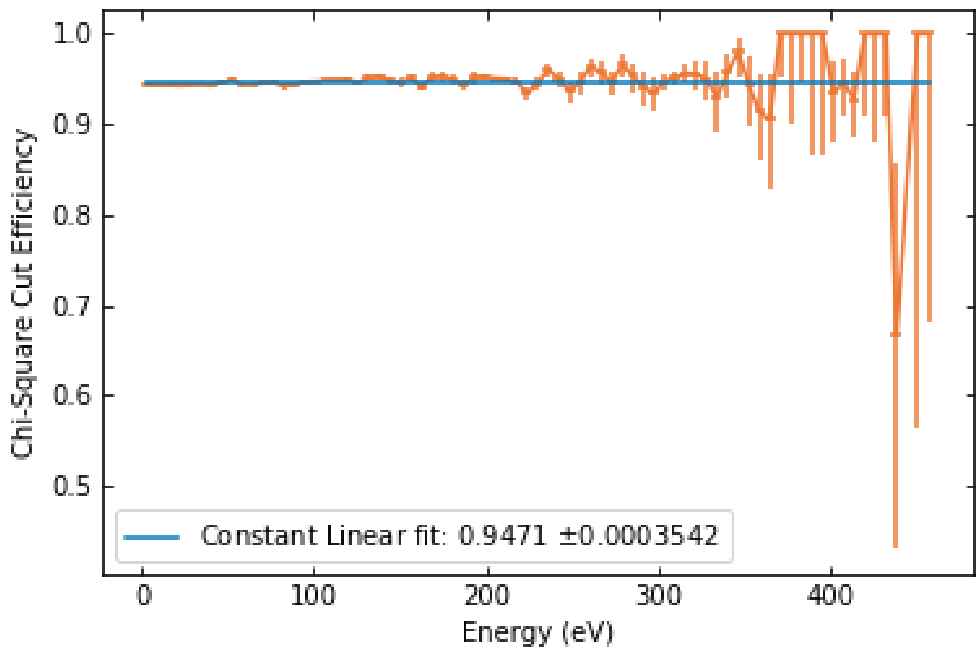


Figure 4-5. The chi-square cut efficiency over the entire analysis window. This cut is set by design to have an energy independent efficiency of approximately 95%.

#### 4.4.2.3 Delta Chi-square Cut

The delta chi-square cut is a cut never previously applied in HVeV analyses, used to remove pile-up events with separations close to the timing resolution of our detector. The delta chi-square reduced quantity is defined as:

Delta Chi-square = Chi-square of single pulse fit - Chi-square of two pulse fit

The single pulse fit is the same OFL RQ used in the chi-square cut, while the two pulse fit is a two template optimum filter fit that looks for the best timings for a two signal fit within 250 samples of the event trigger point. This sample range was chosen because it is the largest range that did not cause excessive additional time in processing the data. This range is wider than required for the purpose of this cut as the regular chi-square cut removes pile-up events with much smaller separations than this. These quantities are calculated in the frequency domain and have a low pass filter applied at 30 kHz to remove high frequency noise. The construction of the delta chi-square RQ is a comparison to tell if the signal at the trigger point better fits one or two resolvable signals, identifying the trigger as a pile-up event or not. Larger delta chi-squared values are more likely to be pile-up events

#### 4.4.2.4 Delta Chi-square Modeling

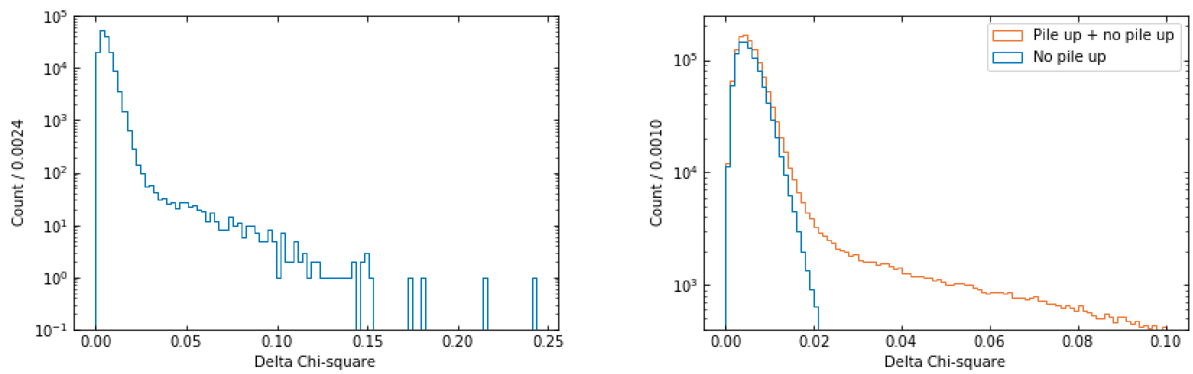


Figure 4-6. (Left) The delta chi-square spectrum of laser data after all existing cuts. (Right) The delta chi-square spectrum for simulated data sets, one with no pile-up and one including pile-up. These are shown to see the effect of pile-up on the delta chi-square spectrum and the similarity between real and simulated data.

To understand the effectiveness of this cut at removing close-time pile-up events, simulated data sets were created using pyCRP, a SuperCDMS software package, with the R3 template and a noise sample from our selected laser data set. Both pile-up and single pulse events were simulated with timing separations ranging from 0-100 samples, all with 1 electron-hole pair energies. This range covers separations much greater than pile-up separations the delta chi-square cut is designed to remove. Below shows the delta chi-square reduced quantity for both selected science data and simulated data sets. The full delta chi-square spectrum is shown on the left with live-times cuts. Comparing this to the delta chi-square spectrum of the simulated data sets (right) we can see that the tail of the simulated data set with pile-up is consistent with the tail seen in our real science data set and it is such events that we want to remove.

#### 4.4.2.5 Delta Chi-square Results

The delta chi-square cut was found to be nearly disjoint from the chi-square cut in the case of run 3 laser data. This is because the laser live-time cuts remove nearly all easily resolvable pile-up events, leaving only signals with poor shape and very close time pile-up. The former is

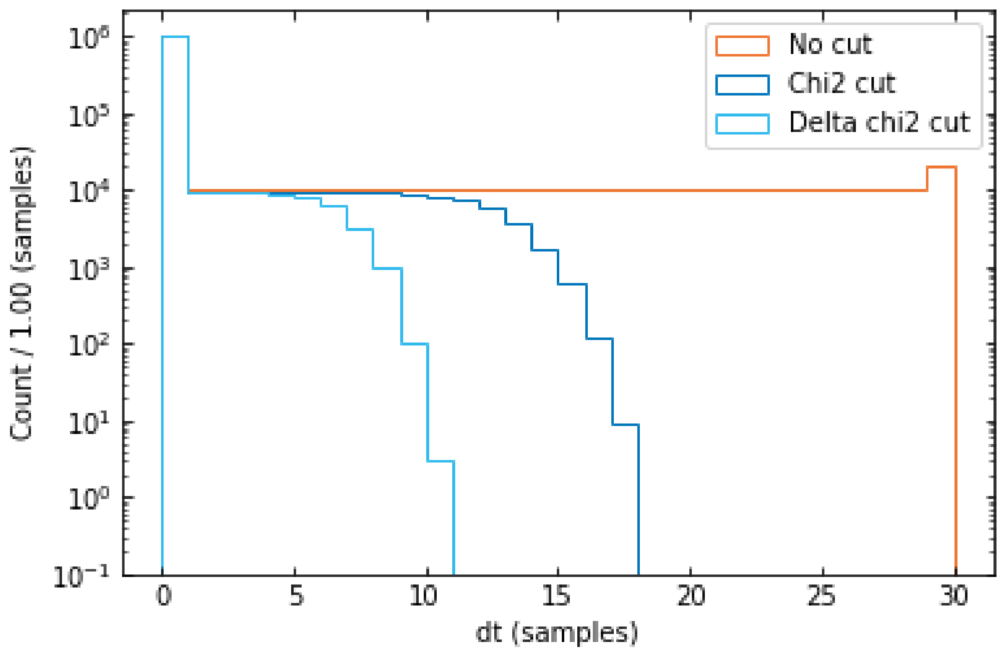


Figure 4-7. The dt spectrum of a simulated data set with and without both data quality cuts. This shows the power of the delta chi-square cut over the chi-square cut removing pile-up events that are closer together in time.

removed by the chi-square cut and the latter by the delta chi-square cut. The delta chi-square cut line and effect on the science data can be seen in Figure 4-8.

## 4.5 Data Calibration

Data calibration involves first accounting for the relative gain between the two channels such that current to energy response in both channels is the same. Then using the laser data sets, and known laser energy, to bring the current scaled data to the energy scale.

### 4.5.1 Relative Channel Weighting

When calculating total signals, we chose to weight the individual channels using the relative weighting factor that provided the best energy resolution for the first electron-hole pair (eh) peak. This was done separately for the NF-H and NF-C detectors using OFL science data. We used science data to avoid the high fraction of sidewall events seen in the laser data, which distorted the shape of the 1-eh peak. Sidewall events should also deposit a higher fraction of energy in the

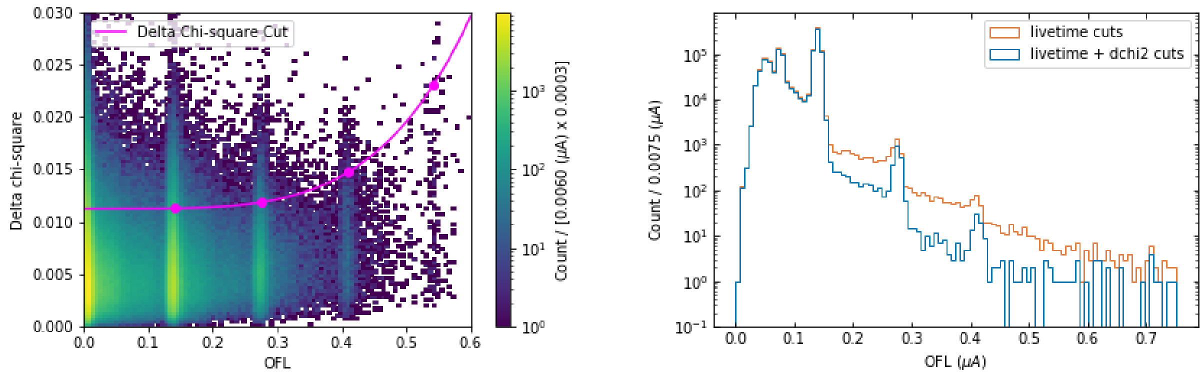


Figure 4-8. (Left) OFL vs. OFL chi-square 2-D histogram of laser data with the delta chi-square cut plotted over. (Right) The OFL spectrum of science data plotted with and without the delta chi-square cut.

outer detector channel than typical science data. The optimization was done before the energy calibration was finalized. Instead, a simple multiplicative calibration was applied to align the first eh peak to 100 eV.

The optimization was also done before any cuts were finalized, so only a simple chi-squared cut was applied. This cut was calculated using a Gaussian fit to the chi-squared distribution in the energy range of interest (between 70 and 130 eV simple calibrated) corresponding to the 1st eh pair. The cut kept data with chi-squared between $\pm 1$ sigma of the Gaussian fit mean. In hindsight, removing events with chi-squared less than the fit mean was unnecessary, but it did not cause any issues either (there were still sufficient events for the calculation).

After the chi-squared cut, another cut was applied to select the first eh peak events more carefully. This was a 2-dimensional cut dependent on both the inner and outer amplitudes. The cut retained events within a 3-sigma ellipse iteratively fit to the data in that space. The cut is 3-sigma under the assumption that the distribution is bivariate normal. In that case, a 3-sigma cut will retain 98.9% of data from the underlying distribution.

The resolution was then calculated by fitting a Gaussian to each weighting factor's distribution. Resolution is proportional to the Gaussian fit's standard-deviation normalized by the Gaussian fit's mean. The resolution vs. weighting was then fit to a model to extract the weighting which gave optimal resolution.

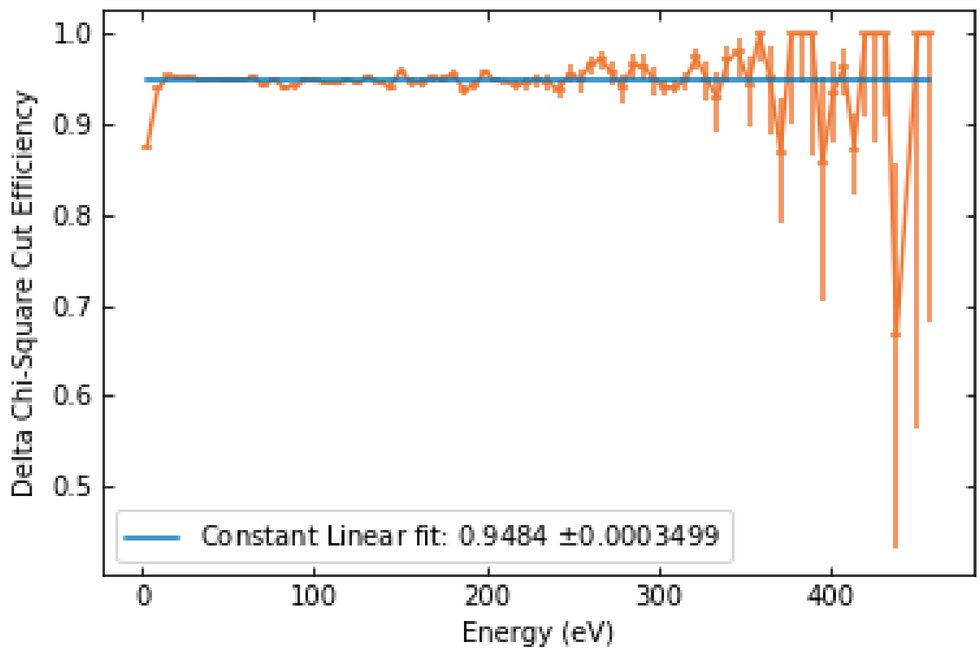


Figure 4-9. The efficiency of the delta chi-square cut applied to the curated laser data set. This is set by design to be energy independent and at approximately 95%.

### 4.5.2 Energy Calibration

As the calibration was preformed on laser data taken at the end of the run, it was important to ensure that the variation in detector gain was small enough throughout the run to be able to do so. To estimate this variation we calculated the single electron-hole pair amplitude in OFL for each day of science data, as well as the overall average of all science data throughout the entire run. The daily gain variation was found to approximately $\pm 0.11\%$ when compared to the average across the entire run. The daily gain variation was fit to an asymmetric Gaussian to estimate the one standard deviation systematic error to be propagated to the overall calibration uncertainty.

Each calibration laser set is corrected for the daily gain variation by scaling the event amplitudes by the ratio of the overall average science data gain to the daily gain of the science data taken from the day each laser set was taken. To these calibration sets we apply the live-time cuts described in Section 4.3.3 as well as the chi-square and delta chi-square data quality cuts described in Sections 4.4.2.1 and 4.4.2.3. Each peak measured in OFL amplitude is fit to a

Gaussian distribution. This is repeated to narrow the fit window to the full-width at half maximum of each so that we only consider the regions that are well described by a Gaussian. The same fitting technique is applied to the OF0 amplitudes for the 0th and 1st peak to determine the offset ($\Delta_0$) discussed later in this section. Additional exponential fits were done to the between peak regions to estimate the possible shifts to peak positions based on the assumption of a non-flat background distribution. These estimates were combined with the peak-fit uncertainties to quantify the total peak uncertainties.

The energy of the *n*th electron-hole pair peak for the laser calibration data is expected to to take the form

$$E_n = n(eV + 1.95\text{eV}) + \Delta_0, \tag{4-4}$$

where $V$ is the NTL gain and $\Delta_0$ is the previously discussed offset. The addition of 1.95 eV is the energy of each photon. The offset is an effect of non-amplified photon events as well as potential further adjustments to this value due to the sidewall trapping discussed in Section 4.3.3. The OF0 RQ is used in addition to OFL to calculate the position of $\Delta_0$ because the time-shifting of OFL allows for the match filtering to better fit to a noise fluctuation nearby a given TTL trigger time for the low amplitude events in the 0th peak.

These offset energies of equation 4-4 are then calibrated to each OFL peak value for three laser data sets simultaneously using a third-order polynomial:

$$E = ax_{\text{OFL}} + bx_{\text{OFL}}^2 + cx_{\text{OFL}}^3. \tag{4-5}$$

The results of this fit can be seen in Figure 4-10. The resulting chi-square per number of degrees of freedom of this fit helps validate the choice of a third-order polynomial for this calibration as this ratio does not show signs of overfitting. The energy residuals for each laser data set's calibrated energy show a fraction of a percent in variation from the combined calibration fit for each peak.

The final calibrated energy spectrum of all Run 3 NF-C science data before and after all

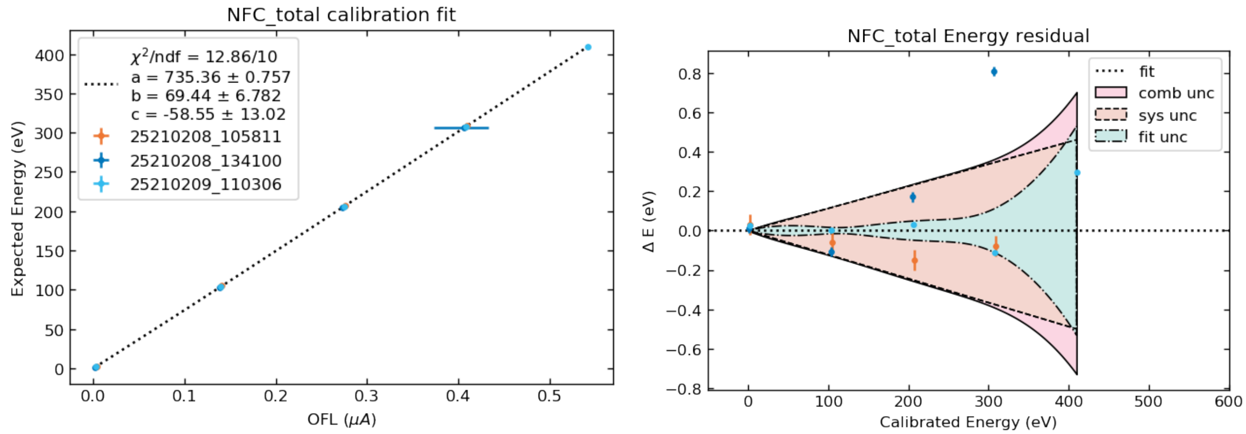


Figure 4-10. (Left) The OFL to energy calibration fit plotted with all laser calibration set points. (Right) The residual of calibrated laser data sets to the expected energies of each peak. This also shows the calibration uncertainties used in the limit setting procedure.

live-time and data quality cuts is shown in Figure 4-11. The double peak below the first electron-hole pair peak is currently interpreted to be due to charge trapping on the side, unpolished surfaces of the detector. The charge trapping effect is discussed later in Section 4.6.2. This is an effect that was also seen in HVeV run 2 and is worth further study for nuclear recoil dark matter searches which consider threshold level events. Fortunately, sub-electron-hole pair signals are not considered in limit setting for electron recoil dark matter searches as limit setting methods only consider events in each electron-hole pair peak.

## 4.6 Signal Modeling and Quantization

In calculating dark matter interaction limits one must develop the expected detector response and resulting event energy spectrums that depend on both the type of dark matter scattering or absorption that is being considered, as well as the medium and interaction detection method. HVeV Run 3 considers four dark matter channels for limit calculations, the same DM models discussed for electronic interactions as those in Section 1.3.3. Dark matter electron scattering that comes in two types depending on the mass of the interaction mediator which vary the interaction rates dependence on momentum transfer. As well as two absorption channels, dark photon absorption and axion-like particle absorption which assumed absorption rates depend on the types of potential dark matter models being considered.

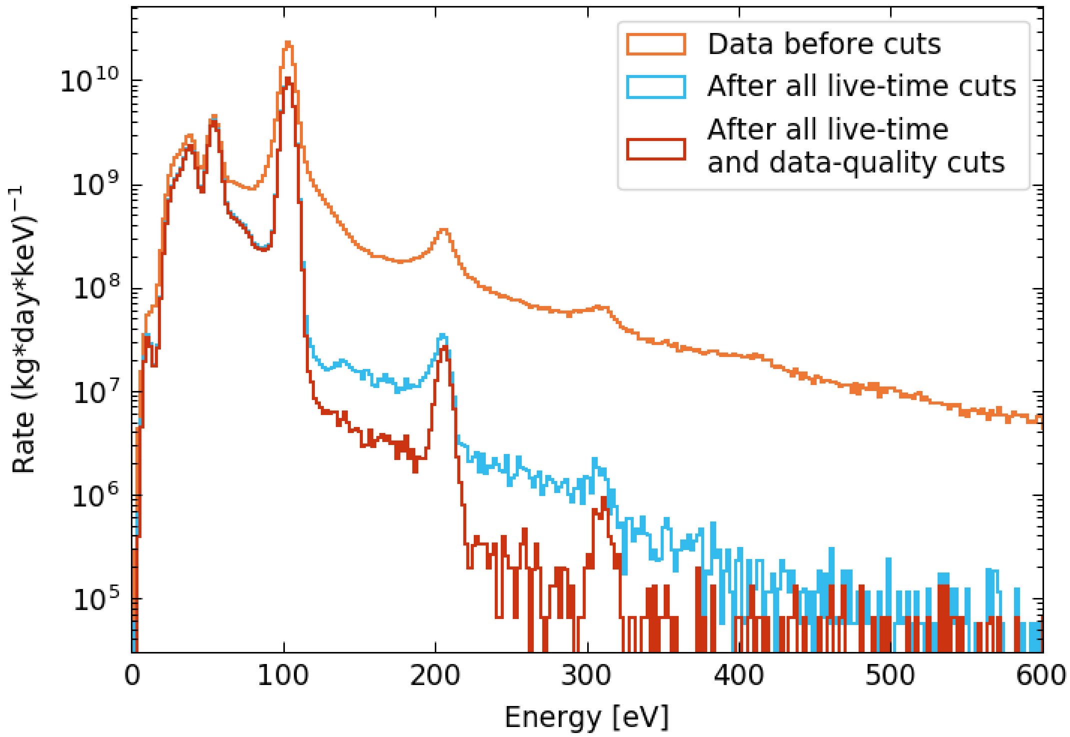


Figure 4-11. The final calibrated energy spectrum of all Run 3 science data with and without cuts.

In the case of Run 3, each interaction rate is dependent upon the energy deposited in the Si crystal, the physical properties of the crystal, and therefore the average number of excited electrons observed in the interaction. This in turn gives an expected rate of the number of electron-hole pairs excited as a function of energy for a given dark matter model with a given mass. This is complicated by concepts such as the energy resolution of the detector or interactions of excited electrons with crystal defects or boundaries which can produce variations in the observed detector response for any same amount energy and momentum deposited by the dark matter particle. This section discusses the interaction rates for the different dark matter models considered in Run 3 and the detector's response to these interactions to develop the signal model of what each dark matter model should look like in this analysis.

### 4.6.1 Detector Energy Resolution

The energy resolution of the detector determines the energy windows for which we consider an event to be part of an electron-hole pair peak and therefore included in the count of events for that peak when calculating the rate for each. HVeV run 2 attempted to calculate detector resolution based on the calibration laser data, however differences between the calculations for the high statistic peaks (1 and 2 electron-hole pairs) found that this was not a suitable correlation. All runs including Run 3 have found an energy dependence to the resolution, increasing with peak number. In addition, the sidewall effect discussed earlier in this chapter made it even more unsuitable to correlate resolution measurements in the laser data to the science data.

Due to these issues the energy resolution must be determined by a combination of science and laser data to determining the electron-hole pair peak windows. After data cuts in science data only the first two peaks' resolutions can be measured with a reasonable uncertainty due to the low statistics in the third peak, and the absence of any measurable fourth peak (statistics remaining around the fourth peak are on the order 1-10 events per bin). Therefore, Run 3 has decided to opt for an energy independent resolution model that includes a large enough systematic uncertainty in our calculations to account for the assumed variations that occur at the higher order peaks.

To estimate the uncertainty band and the nominal energy resolution to use in our calculations we use the baseline energy resolution, as well as the energy resolution of the fourth peak that is measured in our laser calibration data. The baseline energy resolution is calculated on the OF0 amplitude of randomly triggered events in the science data. This gives a lower bound with negligible uncertainty of 3.03 eV. The fourth peak of the laser data is calculated on the large laser data set, but was highly affected by the sidewall effect making it a relatively non-Gaussian peak. Nonetheless, a Gaussian fit was used to estimate the resolution here and produced an upper bound for the resolution of 5.49 eV. The sidewall effect widened this peak making the resolution estimate conservative for the upper bound.

The nominal resolution used is taken to be the average of the lower and upper bounds with a value of 4.26 eV. The real resolutions are most likely lower than this for the first and second peaks and above this for the third and fourth. As it isn't a priori determined which peaks will be used in the limit calculations (this is made clear in Section 4.7), the average seems to be the best value to use for this energy independent estimate.

### 4.6.2 Charge Trapping and Impact Ionization

Two important effects seen in our voltage biased detector setup are charge trapping (CT) and impact ionization (II). These are cases where defects in the crystal either trap (CT) or release extra charge (II) when interacting with the charges ionized by the event interaction. For charge trapping this results in a reduced measurement of energy compared to what should be seen because the event excited charge(s) do not make it across the entire crystal. On the other hand, defects that hold extra charge can instead release extra charge in addition to the event charges when these charges drift across the defect, resulting in an increased energy measurement compared to what should be seen for a given event energy.

In previous HVeV runs, a flat CTII model was considered meaning that for an event that occurs at the surface, there is a constant probability of partial or excess amplification resulting in measured energies between 0 to 200%. To account for events with multiple electron-hole pairs the single electron-hole pair probability distribution function is convolved with itself n times to account for n electron-hole pair events. This model suffers from simplifications of assumption of equal probability of partial amplifications implying an equal depth for which CT can occur, as well as the missing possibility of charges produced from II producing more II charges.

These effects are taken into account with the new CTII model known as the exponential CTII model. In this model we assume an event occurs at the surface and has a mean free path length ($l$) that determines the probability ($p$) of CT or II occurring. These II charges and then also produce new charges to second order. This chain could continue but only up to second order effects are considered. In this model the relations between mean free path and probability of these processes are

$$l_{\mathrm{CTe}} = l_{\mathrm{CTh}} = \frac{-L}{\ln\left(1 - p_{\mathrm{CTe}}\right)}, \tag{4-6}$$

$$l_{\mathrm{IIee}} = l_{\mathrm{IIee}} = l_{\mathrm{IIee}} = l_{\mathrm{IIee}} = \frac{-L}{\ln\left(1 - p_{\mathrm{IIe}}\right)}. \tag{4-7}$$

$L$ is the total length between the two sides of the detectors the electric field is applied across. In this case this length is 4 mm.

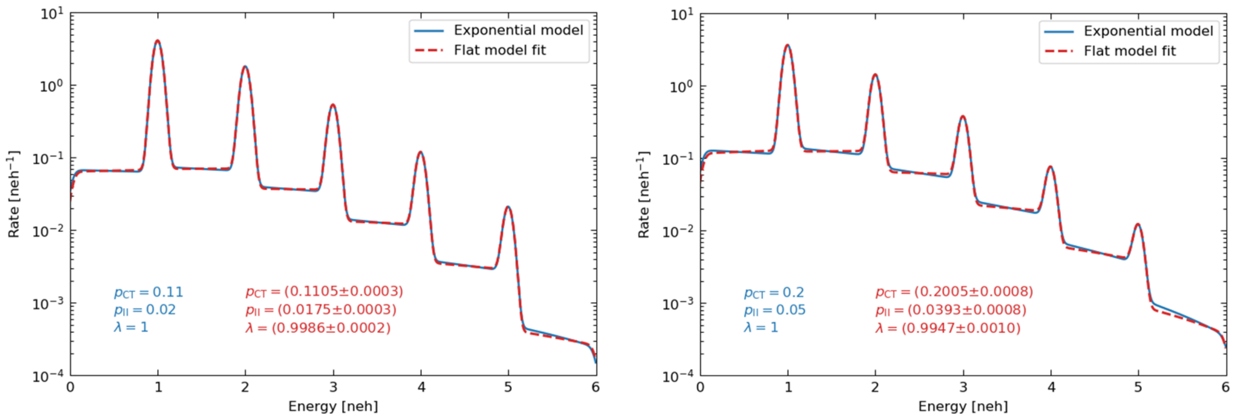


Figure 4-12. Comparison of the exponential and flat CTII models. The left shows with lower CTII probabilities and right with stronger with a more notable deviation from the flat model at high energy (electron-hole pair number).

This model is compared to the flat model in Figure 4-12 and show relatively small difference between the two models. This means that earlier runs were relatively unaffected by the simplifications of the flat model. The difference between the two is seen to increase for larger charge trapping probabilities. However, as the exponential model is more precise we still opt to use it for Run 3. It is also worth noting that in future dark matter searches or other experiments with higher order electron-hole pair peaks present this effect could become more prominent and the flat model may see even greater deviation from the exponential model.

A goal of Run 3 was to provide another source for the probability of charge trapping and impact ionization for the Si wafer that was used to create the detectors used in both run 2 and this run. However, the sidewall effect seen in the laser data made any calculations for this unreliable. Fortunately these the calculations that were made did leave previous measurements of these values within those that were measured in run 2, as well as those from IMPACT. We therefore opted to use the values found in run 2 of $12.8 \pm 1.5\%$ for CT and $1.6\ ^{+1.8}_{-1.6}$ for II.

### 4.6.3 Signal Quantization

The final piece of the building the overall dark matter signal model is the signal quantization model. This is the piece that determines the average number of electron-hole pairs in equation 2-1 that a given event energy should produce which is based on the mean energy of an excited electron-hole pair, as well as the limitation imposed by the band gap energy ($E_{\text{gap}}$) of the detector crystal which imposes a minimum energy to produce an electron-hole pairs at all. In previous HVeV runs, the ratio in equation 2-1 was simply extended to account for the band gap:

$$\langle n_{eh}(E_r)\rangle = \begin{cases} 0 & E_r < E_{\text{gap}} \\ 1 & E_{\text{gap}} < E_r < \varepsilon_{\text{eh}} \\ E_r/\varepsilon_{\text{eh}} & \varepsilon_{\text{eh}} < E_r \end{cases} . \tag{4-8}$$

This simply includes the fact that recoil energies below the band gap energy cannot produce electron-hole pairs and for any recoil less than $\varepsilon_{\text{eh}}$ it is assumed to produce one pair. For any recoil energy higher than this we simply take the ratio. For this case there will therefore be a variance in the number of electron-hole pairs for a given recoil for which previous runs took a measured Fano factor of 0.155 [56] and varied this Fano factor from 0 to 1 in the ionization model to estimate the sensitivity the signal model had to uncertainty in this factor at low energies.

This model is adequate to determine the detector response has been further refined in a new model that has been agreed upon during a recent inter-collaboration held to standardize dark matter search measurements. This model I will refer to as the RK model [57] and first produces a piece-wise function of $\varepsilon_{\text{eh}}$ instead of $n_{eh}$. The overview of the model is:

$$\varepsilon_{\text{eh}}(E_r) = \begin{cases} \infty & E_r < E_{\text{gap}} \\ E_r & E_{\text{gap}} < E_r < 2E_{\text{gap}} \\ \varepsilon_{\text{imp}}(E_r) & E_r \geq 2E_{\text{gap}} \\ \varepsilon_{\text{eh},\infty} & E_r \to \infty \end{cases} . \tag{4-9}$$

For this model the new boundary for the uncertainty in $n_{eh}$ is set at twice the band gap energy. Recoil energies between one and two times the band gap energy are required by conservation of energy to only allow one electron-hole pair excitation. Above twice the band gap, this model describes the uncertainty of the mean electron-hole pair excitation energy as $\varepsilon_{\text{imp}}$

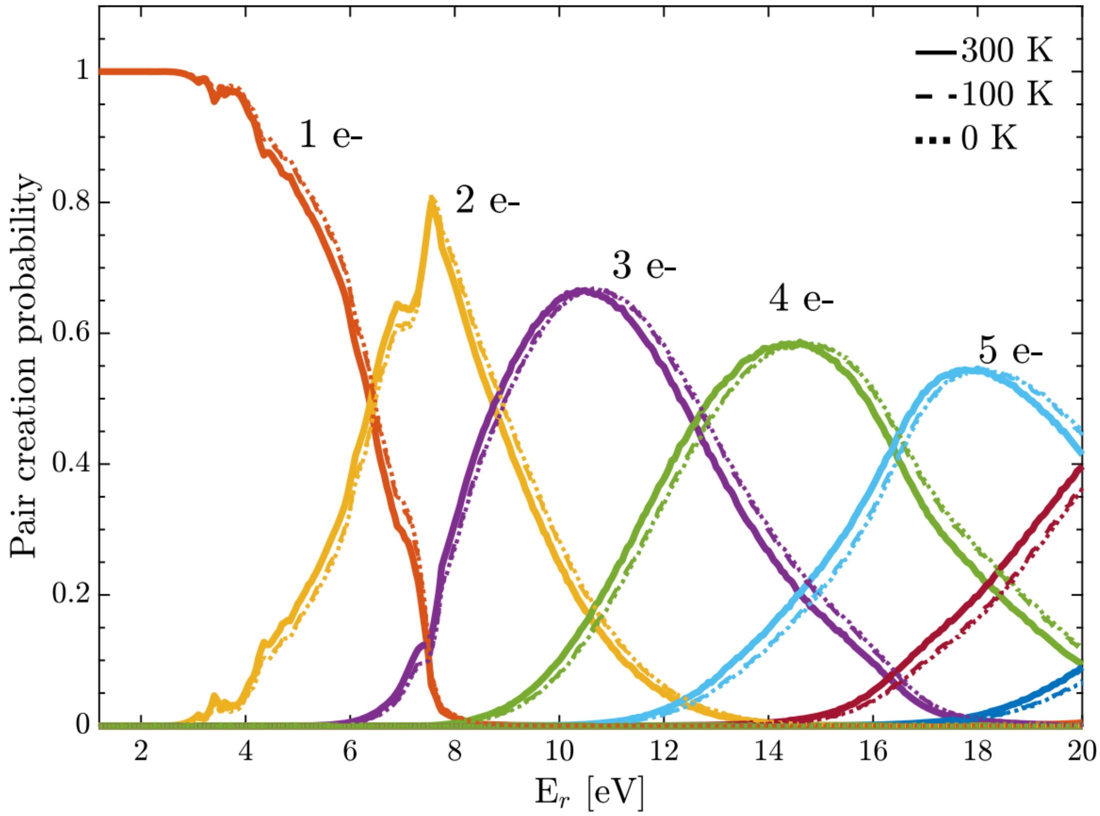


Figure 4-13. The pair creation probabilities for 0 to 20 eV recoil energies created through Monte Carlo simulations. This image is taken from [57].

which is a function of of the recoil energy and is intended to describe $\varepsilon_{\text{eh}}$ at near band gap energies. At energies well above the band gap $\varepsilon_{\text{eh}}$ approaches an asymptotic constant value that this model determines through simulation and is confirmed from previous measurements empirically.

In addition to $\varepsilon_{\text{eh}}$, this model describes the Fano factor of the distribution describing $n_{\text{eh}}$ as a piece-wise function as well:

$$F(E_r) = \begin{cases} 0 & E_r < 2E_{\text{gap}} \\ F_{\text{imp}}(E_r) & E_r \geq 2E_{\text{gap}} \\ F_\infty & E_r \to \infty \end{cases} . \tag{4-10}$$

Again the boundary of uncertainty is at twice the band gap energy as a Fano factor of zero implies zero variance. In the same manner as $\varepsilon_{\text{eh}}$ also sets out to determine the forms for a near gap energy Fano factor, $F_{\text{imp}}$, and in the high energy limit the asymptotic value it approaches $F_\infty$.

At high energies the model identifies $\varepsilon_{\text{eh},\infty}$ and $F_\infty$ to have functional forms:

$$\varepsilon_{\text{eh}} = 1.7E_{\text{gap}} + 0.084A + 1.3 \quad (4\text{-}11)$$

$$F_\infty = -0.028E_{\text{gap}} + 0.0015A + 0.14 \quad (4\text{-}12)$$

These relations introduce the parameter $A$ which is defined as the ratio of the phonon scattering rate divided by the electron scattering rate. In other words, quantifies the likelihood of energy being passed to phonons or other charge carriers in the down-conversion of the recoil energy imparted to the initial interacting charge carrier. Simulations find this ratio to be $A = 5.2$ eV$^2$. Using this result, Monte Carlo simulations are used to extract the pair creation probabilities shown in Fig. 4-13. These probabilities are extended to develop the full signal model used for comparison against the production rates seen during Run 3.

## 4.7 Dark Matter Limits

The final result of a DM search is setting an exclusion limit on the DM-SM interaction parameter vs. DM mass parameter space. This sets the boundary on the interaction parameter DM could possibly hold for a given mass, narrowing the possible forms DM could take. This section discusses the limit setting method used for Run 3 and the final limits that result.

### 4.7.1 Limit setting method

HVeV Run 3 uses the Poisson counting method to compare the number of events measured in each electron-hole pair peak to the expected amount for a given signal model, DM mass, and DM-e interaction rate. This follows from the fact that the DM-e interaction rate is proportional to the scattering cross-section or the square of the coupling constant for absorption interactions:

$$
\begin{aligned}
R &\propto \sigma_{\mathrm{e}}, \\
R &\propto \varepsilon_{\mathrm{eff}}^2, \\
R &\propto g_{\mathrm{ae}}^2.
\end{aligned}
\tag{4-13}
$$

This means that that we can compare the Poisson-determined parameters (subscript $P$) to the reference parameters (subscript 0):

$$
\begin{aligned}
\frac{\sigma_{e,P}}{\sigma_{e,0}} &= \frac{R_P}{R_0}, \\
\frac{\varepsilon_{\mathrm{eff},P}^2}{\varepsilon_{\mathrm{eff},0}^2} &= \frac{R_P}{R_0}, \\
\frac{g_{\mathrm{ae},P}^2}{g_{\mathrm{ae},0}^2} &= \frac{R_P}{R_0},
\end{aligned}
\tag{4-14}
$$

or equivalently we can look at the actual event count (C):

$$
\begin{aligned}
\frac{\sigma_{e,P}}{\sigma_{e,0}} &= \frac{C_P}{C_0}, \\
\frac{\varepsilon_{\mathrm{eff},P}^2}{\varepsilon_{\mathrm{eff},0}^2} &= \frac{C_P}{C_0}, \\
\frac{g_{\mathrm{ae},P}^2}{g_{\mathrm{ae},0}^2} &= \frac{C_P}{C_0}.
\end{aligned}
\tag{4-15}
$$

In this case $C_P$ is the Poisson upper limit on the count with confidence level 0.9 for Run 3. The reference count, $C_0$, is determined by the energy dependent signal model for each electron-hole pair peak ($SM_0^n(E)$):

$$
C_0^n = \int_a^b SM_0^n(E) \cdot eff(E) \cdot X dE. \tag{4-16}
$$

$X$ is the science exposure after live-time cuts and $eff(E)$ is the efficiency function which is designed to be 95% and is calculated to be ∼90% as discussed in Section 4.4.2. As mentioned there, this is designed to be a constant value. The boundaries of integration are determined by the detector energy resolution that in turn defines each peak window at $3\sigma$. This leaves the limits in coupling parameters for a given DM mass to be:

$$\sigma_{e,P} = \frac{C_P^{ab} \cdot \sigma_{e,0}}{X \int_a^b SM_0^{DMe}(E) \cdot eff(E) dE},$$
$$\varepsilon_{\text{eff},P} = \sqrt{\frac{C_P^{ab} \cdot \varepsilon_{\text{eff},0}^2}{X \int_a^b SM_0^{DPA}(E) \cdot eff(E) dE}}, \tag{4-17}$$
$$g_{\text{ae},P} = \sqrt{\frac{C_P^{ab} \cdot g_{\text{ae},0}^2}{X \int_a^b SM_0^{ALP}(E) \cdot eff(E) dE}}.$$

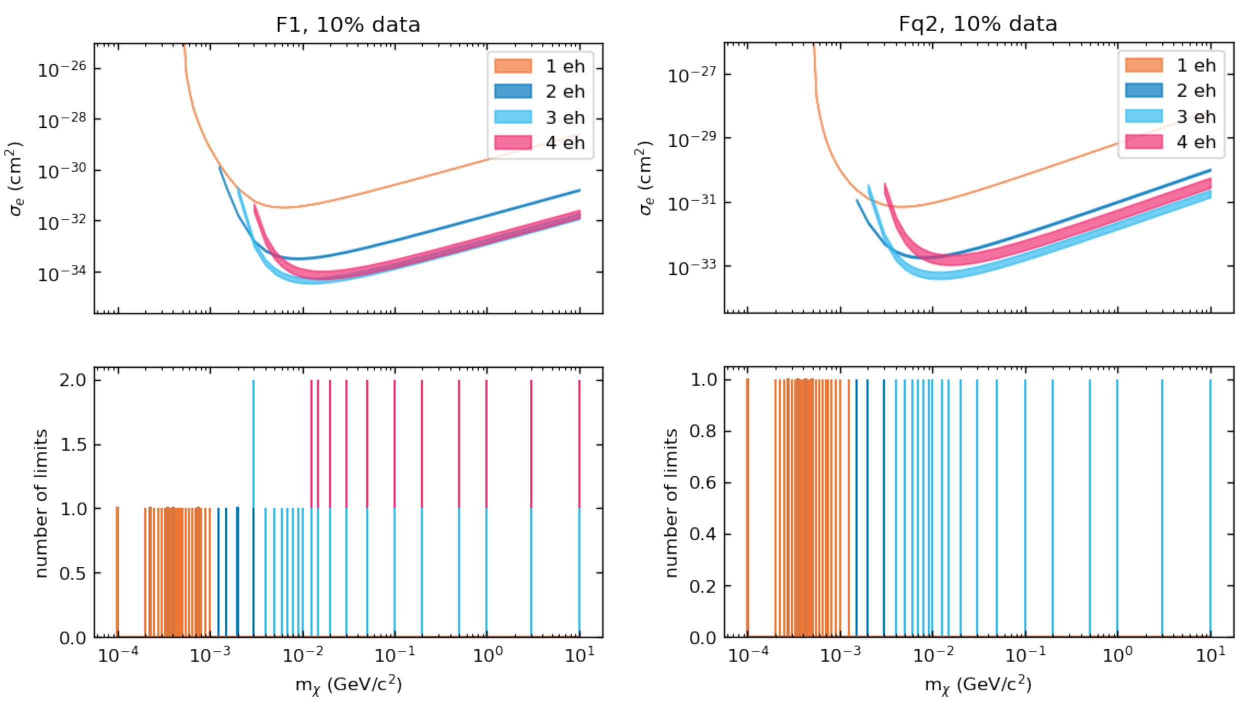


Figure 4-14. The individual peak limits on DM-electron interaction cross-section for a heavy(light) mediator on the left(right). Below shows the peak selections based on each peak limit.

These are the limit set on each peak with a signal only hypothesis. In most cases the variation in these limits between each peak is large enough to only consider the lowest peak. In situations where two peaks produce similar results the confidence interval on counts in each peak

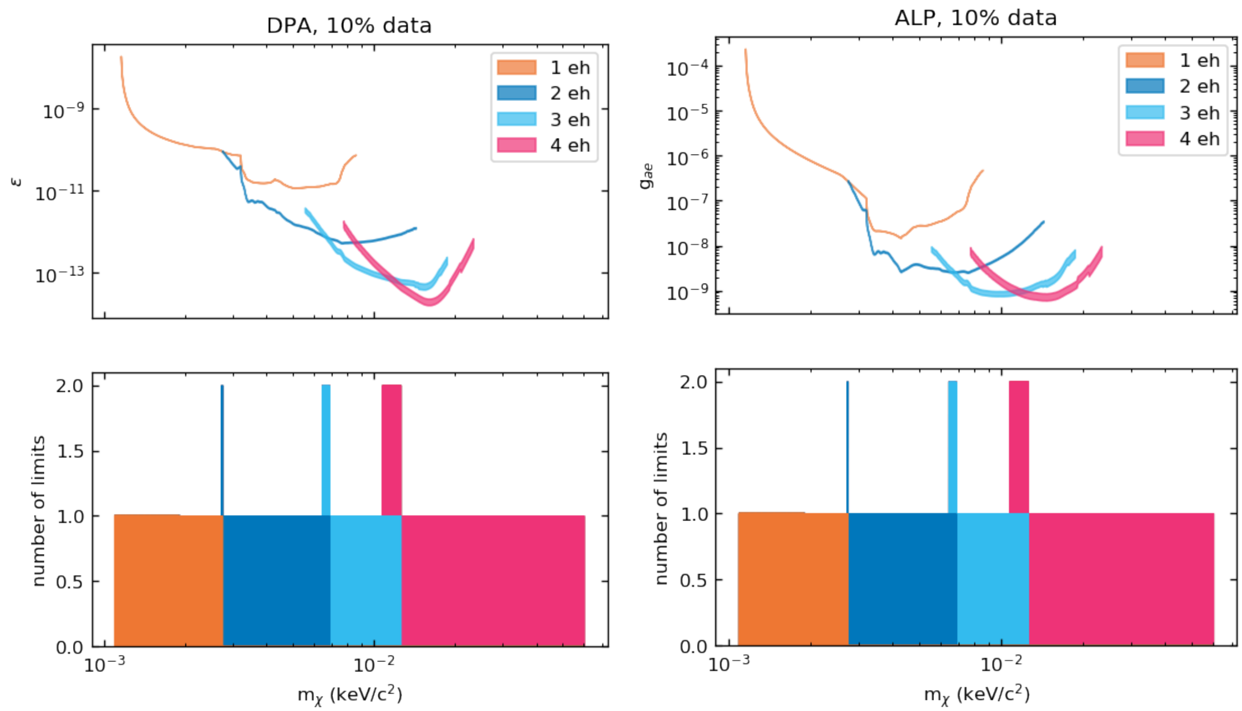


Figure 4-15. The individual peak limits on interaction coupling parameters for the dark photon(ALPs) model on the left(right). Below shows the peak selections based on each peak limit.

must be scaled to account for the use of multiple peaks

$$C_n = c^{1/n}, \tag{4-18}$$

where n is the number of peaks and $c$ is the confidence interval of 90% in counts. This therefore means the individual confidence interval in counts must be set to a higher value in these cases.

In setting these limits it was determined by early preliminary calculations that Run 3 would not be able to produce any world leading limits. Therefore the analysis of Run 3 was focused on developing the analysis techniques for future runs and determining what improvement to detector designs should be considered. As a result of this, we performed a pseudo-blinding technique in our limit setting. A traditional blinding would include stricter limitations in data usage during analysis in addition to data salting techniques. As we were not as concerned with the limits produced as analysis techniques, we instead opted to select 10% of the science data for using for unblinding the remaining 90% of the data. These 10% limits determined the peak selection for setting the final limits and was presented to an internal SuperCDMS collaboration review group for validation of analysis techniques by collaboration members outside the analysis working group. Once validated, the remaining 90% of the data was unblinded. The summary of the limit setting steps are presented below as described by fellow analysis member T. Aralis.

1. Calculate the Poisson limit with a 90% confidence level assuming for each eh interval

   (a) The number of observed events, $N_{\text{obs}}$, is a statistical under-fluctuation, and adjust the number of events to $N'_{\text{obs}}$ such that $N'_{\text{obs}} - \sigma_{N'_{\text{obs}}} = N_{\text{obs}}$.

   (b) The number of observed events, $N_{\text{obs}}$, is a statistical over-fluctuation, and adjust the number of events to $N'_{\text{obs}}$ such that $N'_{\text{obs}} - \sigma_{N'_{\text{obs}}} = N_{\text{obs}}$.

2. Repeat the previous step, but scaling both the exposure and $N'_{\text{obs}}$ by a factor of 9.

3. For each electron-hole pair number, determine if its best-case limit (over-fluctuation assumption) is lower than all other electron-hole pair number's worst-case limit (under-fluctuation assumption). Compile a list of all electron-hole pair number that satisfy this. These electron-hole pair number have at least one scenario, given the under- or over-fluctuation assumptions, where they set the best limit, and should be included.

4. The individual electron-hole pair limits to consider will be the ones considered for current exposure, OR the ones considered for the scaled exposure.

5. For n limits that are considered, calculate the confidence level for each electron-hole pair limit using eqn. 4-18.

6. Recalculate the Poisson limit with the confidence levels determined in the previous step.

7. Determine the lowest limit by comparing only the electron-hole pair limits considered from step 4.

$\sigma_{N'_{obs}}$ is the one standard deviation from the Poisson distribution such that $\sigma_{N'_{obs}} = \sqrt{N'_{obs}}$. Figures 4-14 and 4-15 show the results of this peak selection process which chooses the peak(s) that are to be used in the final limit setting. DM masses where the interaction limit bands overlap are regions in which more than one peak is considered for the final limit setting.

### 4.7.2 Dark Matter Limits

The final unblinded interaction limits are shown in Figures 4-16 and 4-17. These limits are plotted against results from other DM search experiments, as well as the limits found in previous HVeV runs. Though these limits do not span any new parameter space compared to other experiments, we do see some improvement compared to previous HVeV runs. The difference in extent of reach to higher masses between Run 2 and Run 3 for the absorption models is that Run 2 data included events up to the sixth electron-hole pair peak.

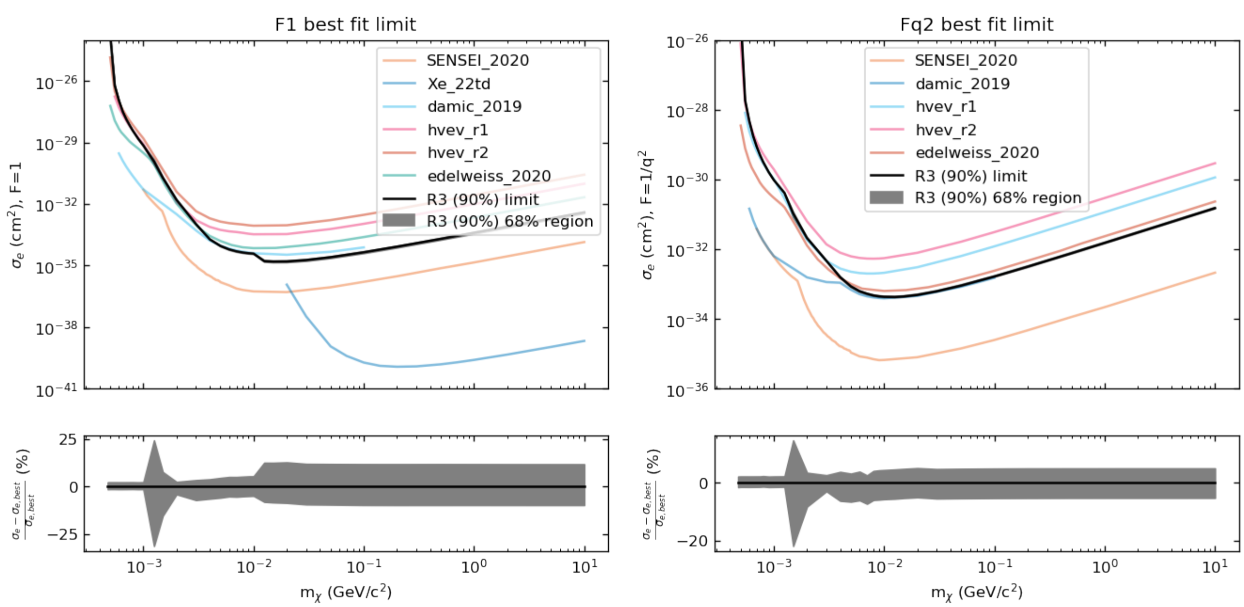


Figure 4-16. The final 90% limits on DM-electron interaction cross-section for a heavy(light) mediator on the left(right), plotted against other leading DM search experiments, as well as previous HVeV runs. Below shows the fractional width of the limit setting bands for each.

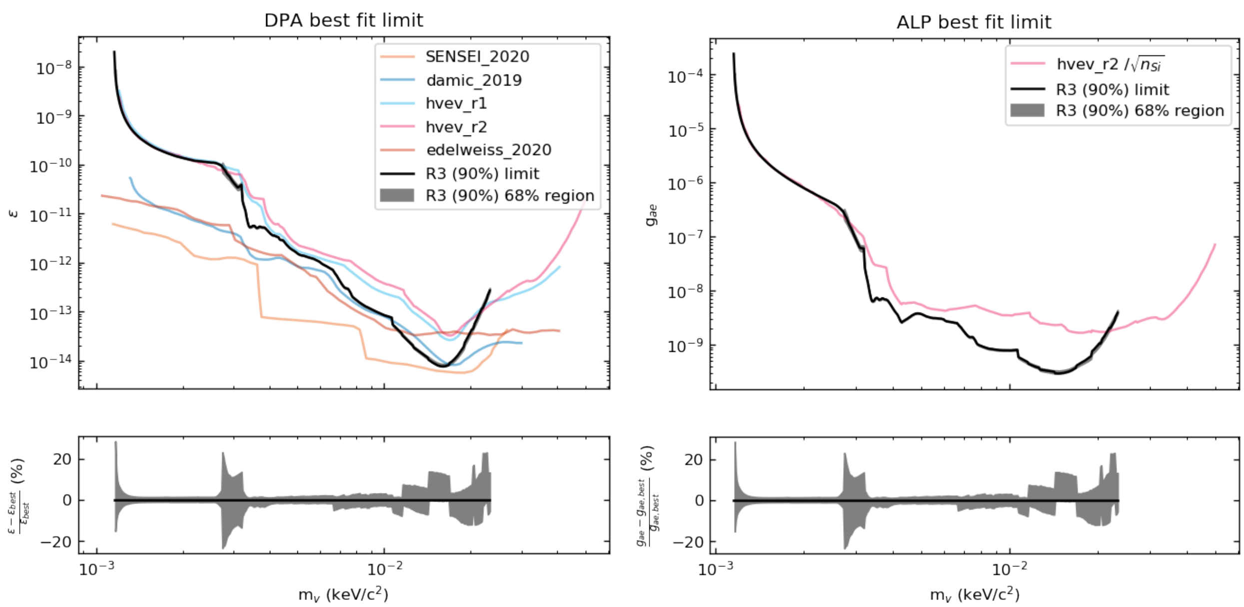


Figure 4-17. The final 90% limits on interaction coupling parameters for the dark photon(ALPs) model on the left(right)), plotted against other leading DM search experiments, as well as previous HVeV runs. Below shows the fractional width of the limit setting bands for each.

# CHAPTER 5
# SUMMARY AND FUTURE WORK

The search for DM in the sub-GeV range presents new challenges in both detector design and and subsequent data analysis. The IMPACT measurement made at TUNL is a first step in nuclear recoil experiments extending to this lower mass regime. These measurements are the first that extend all the way down to 100 eV and enable analysis through the entire projected sensitivity of SuperCDMS SNOLAB. HVeV run 3 saw a mixed bag of success in the third DM-electronic recoil search using HVeV detectors produced by SuperCDMS. We did not produce any world leading limits but found much success in improving data analysis and using multiple detector chip for coincidence analysis and background event rejection.

## 5.1 Future Work for IMPACT

IMPACT at TUNL was the first run in a line of measurements projected for the IMPACT project. After the measurement at TUNL, the HVeV detector system was transported to the University of Montreal for follow up measurements there. The measurement at TUNL was the first that extended to such small recoil energies and it is important to both validate and explore any possible remaining dependencies the ionization yield may have. Further analysis of the IMPACT at TUNL data is still underway to try and get all we can out of the data. Future runs include performing similar measurements in Ge which is also assumed to deviate from Lindhard theory at sub-keV energies.

## 5.2 Future Work for HVeV Electronic Recoil Searches

Data for the fourth HVeV has already been taken at NEXUS and analysis of this data is underway. Run 3 suggested that the discussed burst events were from luminescence in the detector cavity and postulate this was sourced from scintillation on the PCB detector holders. A new detector holder design was implemented in this run and has already shown reduced burst event frequency. This run also has the the advantage of using two detectors with NF-C masks, the best performing mask in run 3, and two other detector chips that have both been successfully ran at NEXUS. This shows promise that some of the set backs seen in Run 3 have been solved for this next round of DM searches.

LIST OF REFERENCES


[1] F. Zwicky, Helvetica Physica Acta **6**, 110 (1933).

[2] E. Hubble and M. L. Humason, **74**, 43 (1931).

[3] V. C. Rubin and J. Ford, W. Kent, **159**, 379 (1970).

[4] M. Roberts and R. Whitehurst, **201**, 327 (1975).

[5] M. Roberts and A. Rots, **26**, 483 (1973).

[6] D. Rogstad and G. Shostak, **176**, 315 (1972).

[7] Y. Sofue and V. Rubin, Annual Review of Astronomy and Astrophysics **39**, 137 (2001).

[8] M. Milgrom, **270**, 365 (1983).

[9] J. Bekenstein and M. Milgrom, **286**, 7 (1984).

[10] J. D. Bekenstein, Phys. Rev. D **70**, 083509 (2004).

[11] D. Clowe, M. Bradač, A. H. Gonzalez, M. Markevitch, S. W. Randall, C. Jones, and D. Zaritsky, The Astrophysical Journal **648**, L109 (2006).

[12] P. Collaboration and Aghanim *et al.*, **641**, A6 (2020), arXiv:1807.06209 [astro-ph.CO] .

[13] E. O. Nadler (DES Collaboration), Phys. Rev. Lett. **126**, 091101 (2021).

[14] K. Griest and M. Kamionkowski, Phys. Rev. Lett. **64**, 615 (1990).

[15] G. Jungman, M. Kamionkowski, and K. Griest, Physics Reports **267**, 195 (1996).

[16] S. Tulin and H.-B. Yu, Physics Reports **730**, 1 (2018).

[17] E. W. Kolb and M. S. Turner, *The Early Universe*, Vol. 69 (1990).

[18] X. Chu, T. Hambye, and M. H. Tytgat, Journal of Cosmology and Astroparticle Physics **2012** (05), 034.

[19] C. Dvorkin, T. Lin, and K. Schutz, Physical Review Letters **127**, 10.1103/physrevlett.127.111301 (2021).

[20] L. J. Hall, K. Jedamzik, J. March-Russell, and S. M. West, Journal of High Energy Physics **2010**, 10.1007/jhep03(2010)080 (2010).

[21] R. D. Peccei and H. R. Quinn, Phys. Rev. Lett. **38**, 1440 (1977).

[22] R. D. Peccei and H. R. Quinn, Phys. Rev. D **16**, 1791 (1977).

[23] M. Pospelov, A. Ritz, and M. Voloshin, Phys. Rev. D **78**, 115012 (2008).

[24] G. Bertone and D. Hooper, Reviews of Modern Physics **90**, 10.1103/revmodphys.90.045002 (2018).

[25] B. Carr, F. Kühnel, and M. Sandstad, Phys. Rev. D **94**, 083504 (2016).

[26] B. Penning, Journal of Physics G: Nuclear and Particle Physics **45**, 063001 (2018).

[27] G. Aad *et al.*, The European Physical Journal C **75**, 10.1140/epjc/s10052-015-3517-3 (2015).

[28] V. Khachatryan *et al.*, The European Physical Journal C **75**, 10.1140/epjc/s10052-015-3451-4 (2015).

[29] Aguilar-Arevalo *et al.* (The MiniBooNE-DM Collaboration), Phys. Rev. D **98**, 112004 (2018).

[30] A. Albert *et al.*, T. Fermi-LAT, and D. Collaborations), The Astrophysical Journal **834**, 110 (2017).

[31] R. Essig, E. Kuflik, S. D. McDermott, T. Volansky, and K. M. Zurek, Journal of High Energy Physics **2013**, 10.1007/jhep11(2013)193 (2013).

[32] G. Giesen, M. Boudaud, Y. Génolini, V. Poulin, M. Cirelli, P. Salati, and P. D. Serpico, Journal of Cosmology and Astroparticle Physics **2015** (09), 023.

[33] M. Boudaud, J. Lavalle, and P. Salati, Phys. Rev. Lett. **119**, 021103 (2017).

[34] Albert *et al.* (ANTARES Collaboration and IceCube Collaboration), Phys. Rev. D **102**, 082002 (2020).

[35] F. Donato, N. Fornengo, and S. Scopel, Astroparticle Physics **9**, 247 (1998).

[36] J. I. Read, Journal of Physics G: Nuclear and Particle Physics **41**, 063101 (2014).

[37] J. Lewin and P. Smith, Astroparticle Physics **6**, 87 (1996).

[38] R. Essig, M. Fernandez-Serra, J. Mardon, A. Soto, T. Volansky, and T.-T. Yu, Direct detection of sub-gev dark matter with semiconductor targets (2016), arXiv:1509.01598 [hep-ph] .

[39] T. Trickle, Z. Zhang, K. M. Zurek, K. Inzani, and S. M. Griffin, Journal of High Energy Physics **2020**, 10.1007/jhep03(2020)036 (2020).

[40] Y. Hochberg, T. Lin, and K. M. Zurek, Phys. Rev. D **95**, 023013 (2017).

[41] Y. Hochberg, T. Lin, and K. M. Zurek, Physical Review D **95**, 10.1103/physrevd.95.023013 (2017).

[42] I. M. Bloch, R. Essig, K. Tobioka, T. Volansky, and T.-T. Yu, Journal of High Energy Physics **2017**, 10.1007/jhep06(2017)087 (2017).

[43] Agnese *et al.* (SuperCDMS Collaboration), Phys. Rev. Lett. **112**, 241302 (2014).

[44] F. Duncan, A. Noble, and D. Sinclair, Annual Review of Nuclear and Particle Science **60**, 163 (2010), https://doi.org/10.1146/annurev.nucl.012809.104513 .

[45] N. Kurinsky, P. Brink, R. Partridge, B. Cabrera, and M. Pyle, Supercdms snolab low-mass detectors: Ultra-sensitive phonon calorimeters for a sub-gev dark matter search (2016), arXiv:1611.04083 [physics.ins-det] .

[46] R. Agnese *et al.* (SuperCDMS Collaboration), Phys. Rev. D **95**, 082002 (2017).

[47] N. A. Kurinsky 10.2172/1472104 (2018).

[48] J. Lindhard, V. Nielsen, M. Scharff, and P. V. Thomsen, Kgl. Danske Videnskab., Selskab. Mat. Fys. Medd. .

[49] M. C. Pyle 10.2172/1127926 (2012).

[50] K. Irwin and G. Hilton, Transition-edge sensors, in *Cryogenic Particle Detection*, edited by C. Enss (Springer Berlin Heidelberg, Berlin, Heidelberg, 2005) pp. 63–150.

[51] D. Brown *et al.*, Nuclear Data Sheets **148**, 1 (2018), special Issue on Nuclear Reaction Data.

[52] C. Lee and X.-L. Zhou, Nuclear Instruments and Methods in Physics Research Section B: Beam Interactions with Materials and Atoms **152**, 1 (1999).

[53] Amaral *et al.*, Phys. Rev. D **102**, 091101 (2020).

[54] A. E. e. a. Chavarria, Phys. Rev. D **94**, 082007 (2016).

[55] A. N. Villano, M. Fritts, N. Mast, S. Brown, P. Cushman, K. Harris, and V. Mandic, Phys. Rev. D **105**, 083014 (2022).

[56] A. Owens, G. Fraser, and K. J. McCarthy, Nuclear Instruments and Methods in Physics Research Section A: Accelerators, Spectrometers, Detectors and Associated Equipment **491**, 437 (2002).

[57] K. Ramanathan and N. Kurinsky, Phys. Rev. D **102**, 063026 (2020).

## BIOGRAPHICAL SKETCH

Corey first became particularly interested in physics in high school. All his life he had planned on being a scientist of some sort but wasn't sure until then. For some reason silly experiments like calculating how long a piece of elastic was necessary to have a bungee jumping barbie not smash its plastic skull really drove the decision home. Or more so when the protractor really wasn't doing the job for measuring the angle of your box car's slope, so he made his first calibration by measuring the response of the system to a known mass to find the correct angle and successful applied the correct mass to accelerate it across the system in one second on the first try.

Corey attended an international school in Japan for his first year of college to get out and see the world, but soon realized continuing at a primarily business school wouldn't help him in a science career (he probably always knew, but Japan ya know?). A brief break followed before starting his BS in physics at the University of South Florida. He focused on astronomy and astrophysics throughout undergrad, attending two different research experiences for undergraduates at the Very Large Array radio telescope and Seoul National University studying gamma ray bursts and pulsar glitches respectively.

Following undergraduate Corey was uncertain with his career in further academia and took several years to work and feel things out. Finally in 2015 Corey decided to apply for graduate school and was accepted to the University of Florida in 2016. At this time he was still uncertain about a career in physics, but still had the desire to learn how the universe works at a fundamental level and decided to give it a go regardless. He entered Dr. Tarek Saab's lab approximately three years later. He received his Ph.D. from the University of Florida in the spring of 2023.